Temporal and spatial variations in uplift from river-profile inversions at the Central Anatolian Plateau southern margin

Simone Racano[1,2], Taylor F. Schildgen[1,3], Domenico Cosentino[2], Scott R. Miller[4]

[1] *Helmholtz-Zentrum Potsdam, Deutsches GeoForschungsZentrum GFZ, Telegrafenberg Potsdam, Germany*

[2] *Roma Tre University, Rome, Italy*

[3] *University of Potsdam, Potsdam, Germany*

[4] *University of Utah, Salt Lake City, Utah, USA*

Keypoints:

- *Linear inversion of longitudinal river profiles for the Central Anatolian Plateau southern margin uplift history;*
- *The drainage system records a strong middle Pleistocene uplift pulse that affected the margin of the plateau;*
- *Evidence of eastward migration of the uplift pulse through time;*
- *Possible relation between uplift timing and rates with the break-off of the Cyprus slab.*

ABSTRACT

The Central Anatolian Plateau (CAP) southern margin experienced a strong uplift pulse with max. rates of 3.5 km/Myr during the Quaternary, based on marine sediments dated to the Middle Pleistocene that are now located at 1500 m.a.s.l. In geodynamically active areas, spatio-temporal variations in uplift can provide key insights into the processes responsible for the evolution of topography. Fluvial landscapes record elements that reflect temporal and spatial variations in rock uplift rates, such as the normalized river steepness index, which is affected by rock uplift rates, the erodibility of the underlying rock, and factors such as climate. Following the calibration of river profiles for an erosion coefficient value, which can be done using independent data (in our case, uplifted marine terraces), river profiles can be inverted for the uplift histories that created them. In our study, we demonstrate how it is possible to define the spatio-temporal uplift history of the CAP southern margin by quantitative analysis of multiple river profiles. Our results, which show a wave of rapid uplift propagating from west to east during the Quaternary and subsequent exponential decreases in uplift rates, provide support for Quaternary uplift being driven by tearing and break-off of the Cyprus slab.

***Keywords**: Central Anatolian Plateau, Quaternary uplift, river linear inversion, slab break-off*

1. <u>Introduction</u>

High-elevation, low relief plateaus, such as the Himalayan-Tibetan Plateau and the Altiplano-Puna Plateau, represent singular topographic features on the Earth surface, often considered responsible for both local and global climate changes (Ruddiman & Kutzbach, 1989; Molnar et al., 1993; Lenters & Cook, 1997; Gregory-Wodzicki, 2000; Zhisheng et al., 2001; Hartley, 2003; Harris, 2006; Strecker et al., 2007; Ehlers & Poulsen, 2009). The eastern Mediterranean region hosts one of the main orogenic plateaus of the Western Alpine-Himalayan orogenic belt, the Central Anatolian Plateau (CAP), which resulted from the collision between Arabia with Eurasia starting at circa 20 Ma (Ballato et al., 2011; Okay et al., 2010) along the Bitlis-Zagros thrust zone. The mechanisms that led to the CAP uplift remain debated, but have primarily been attributed to crustal and upper mantle dynamics related to interactions among the Eurasian, African and Arabian plates (Faccenna et al., 2006; Biryiol et al., 2010; Cosentino et al., 2012; Schildgen et al., 2012a-b; 2014; Bartol & Govers, 2014; Goğuş et al., 2017; Meijers at al., 2018; Öğretmen et al., 2018a; McPhee et al., 2019; Fernandez-Blanco et al., 2019; 2020; Racano et al., 2020). Considering that the plateau margins rise high above the plateau interior in Central Anatolia, different mechanisms are likely responsible for uplift of the plateau margins and the plateau interior.

A number of observations constrain the uplift history of the CAP. In Central Anatolia, $\delta^{18}O$ analysis of Oligo-Miocene lacustrine carbonates suggests the absence of significant orographic barriers at both the northern and southern plateau margins prior to 20–16 Ma (Lüdecke et al., 2013). A steady decrease in $\delta^{18}O$ values between ca. 11 and 5 Ma was interpreted to indicate late Miocene surface uplift of the CAP southern margin (Meijers et al., 2018). Schildgen et al. (2012a) used uplifted marine sediments and qualitative river-profile analysis to suggest two main uplift phases at the southern margin: an initial slower uplift phase starting after ca. 8 Ma, and a more rapid phase after ca. 1.6 Ma. Stratigraphical analysis has been used to refine the timing of these two main uplift phases, the first at the end of the Miocene (5.45 to 5.33 Ma, Radeff et al., 2017), and the second during the Middle Pleistocene (after 0.467 Ma, Öğretmen et al. 2018a). Modelling of the marine terrace evolution along the CAP southern margin indicates the Middle Pleistocene event occurred during MIS7 (210-240 ka), with maximum uplift rates estimated around 3.4-3.8 km/Myr (Racano et al., 2020).

Despite these constraints on the uplift history, uncertainties remain concerning the detailed spatio-temporal evolution of topography, which can be used to test various proposed uplift mechanisms. Recent studies have related uplift of the southern CAP and Cyprus to thermo-viscous forearc uplift associated with subduction, whereby compression led to the mechanical, brittle, upper-crustal strain that created the Cyprus forearc system, and also the thermal, ductile, lower-crustal deformation that propelled CAP growth (Férnandez-Blanco et al., 2019; 2020). These studies predict the gradual growth of topography to kilometer-scale heights in the Central Taurides before the Pliocene (Fernández-Blanco, 2019; 2020; Meijers et al., 2018). Alternative proposed mechanisms for uplift of the CAP southern margin include continental collision (McPhee & van Hinsbergen, 2019), or break-off of the Cyprus slab (Cosentino et al., 2012; Schildgen et al., 2012a-b; Radeff et al., 2016, 2017) with a majority of the modern topography having been created since the middle Pleistocene

(Öğretmen et al., 2018a; Racano et al., 2020). The latter mechanism could result in a pulse of brief, but rapid uplift (i.e., several km/Myr for less than 1 Myr), if the break-off event is relatively shallow (Duretz & Gerya, 2013). Furthermore, if a slab break-off event occurs through lateral progression of a slab tear, the uplift history could show a spatio-temporal pattern that mimics the propagation of the tear. This spatio-temporal pattern of uplift would contrast with a slower, prolonged, and spatially continuous pattern of uplift associated with crustal thickening linked to subduction-induced strain or continental collision.

Topography presents a useful test of these differing proposed uplift histories. Because tectonics and topography are strongly linked in regions that have experienced recent deformation, the topography of the CAP can be used to evaluate the predictions of the various geodynamical models. Such a record is commonly expressed in longitudinal profiles of rivers, which can be used to quantiatively assess spatial and temporal patterns of uplift (Kirby & Whipple, 2012). A growing endeavor in tectonic geomorphology is to infer the rock-uplift (or base-level fall) history by inverting river profiles. Because the position of a point along a river profile is defined by the balance between uplift and erosion, and perturbations to the uplift rate tend to propagate upstream along the profile (e.g., Howard & Kerby, 1983;Tucker & Slingerland, 1996; Whipple et al, 1999), along-channel variations in gradient can be inverted for an uplift history if certain testable assumptions about the mechanisms of fluvial erosion are met (Pritchard et al, 2009; Roberts & White, 2010; Roberts et al., 2012a-b; Goren et al., 2014; Fox et al, 2014, 2015; McNab et al., 2018; Gallen, 2018; Li et al., 2020; Ma et al., 2020).

McNab et al. (2018) used river-profile inversions throughout Anatolia, together with a compilation of basalt geochemistry and ages, to infer that elevated aesthenospheric temperatures coupled with thinned lithosphere played an important role in uplift of the region as a whole. In this paper, we present a more spatially focused analysis of the morphostructural and fluvial features of the CAP southern margin to explore spatial-temporal variations in uplift rates during the Quaternary. The analyses comprise both regional assessments of topographic metric variations and calibrated linear inversions of river profiles to infer uplift histories, and particularly how those histories vary spatially along the CAP southern margin. Finally, we use our results to assess the which geodynamic mechanism best explains the Quaternary evolution of the CAP southern margin.

2. Regional tectonic setting and uplift history

The tectonic setting of central Anatolian is a consequence of the convergence of the African and Arabian plates relative to the Anatolian plate (Reilinger et al., 1997). The stresses between the plates are partly compensated by the westward movement of the Anatolian plate along North Anatolian and East Anatolian Fault Zones (Ketin, 1948; McKenzie, 1978; Dewey & Şengör, 1979; Şengör, 1980; Şengör et al., 1985; Burke & Şengör, 1986; Barka & Kadinsky-Cade, 1988). Several intraplate tectonic elements delimit the CAP (Fig. 1), separating it from the contractional Eastern Anatolian Plateau and the predominantly extensional Western Anatolian Province (Büyüksaraç et al., 2005). At the eastern CAP limit, the transtensive Ecemiş and Kozan faults continue offshore to become the transtensive Silifke-Anamur Fault Zone. The western CAP limit is also defined by two major transtensive faults, the Kirkkavak and the Aksu-Kyrenia faults(Aksu et al., 2005; 2014; Güneş et al., 2018)(Fig. 1).

2.1 Uplift constraints of the CAP margins

The northern and southern margins of the CAP show substantial differences in their Quaternary uplift histories. Uplift at the northern margin of the CAP has been explained by crustal thickening along a restraining bend in the North Anatolian fault zone, resulting in uplift rates from 0.2-0.3 km/Myr since ca. 0.4 Ma within the Central Pontides based on marine and river terraces (Yıldırım et al., 2013a-b). Terraces near the Kızılırmak River outlet yielded similar uplift rates of 0.28 ± 0.07 km/Myr since 545 ka (Berndt et al., 2018). Within the east-central part of the plateau interior, Çiner et al. (2015) used fluvial terraces of the northward draining Kızılırmak River to estimate a mean rate of 0.051 km/Myr for the last 1.9 Ma.

In contrast, the southern margin appears to show a faster and more complex uplift history divided into two main stages. Stratigraphical analysis in the Adana-Cilicia basin, south-east of the CAP southern margin, indicates the deposition of ~1.7 km of clastic sediments derived from the Central Taurides, corresponding to the first uplift phase of the CAP southern margin at the end of the Messinian, ca. 5.45 to 5.33 Ma. (Radeff et al., 2016, 2017; Öğretmen et al., 2018a). The second, faster uplift phase has been constrained by biostratigraphic and morphostratigraphical analyses. On land, rapid uplift is indicated by the presence of early Pleistocene (Calabrian) to middle Pleistocene marine sediments capping the margin together with a paleoshoreline at a maximum elevation of 1400-1500 m.a.s.l. dated at 0.467 Ma (Öğretmen et al., 2018a), and a staircase sequence of surfaces from the top of the margin toward the sea that have been interpreted as marine terraces (Racano et al., 2020). These terrestrial deposits and landforms indicate that a pulse of fast uplift occurred during the middle Pleistocene (MIS7), with maximum uplift rates estimated to have been 3.4 to 3.8 km/Myr (Racano et al., 2020).

2.2 Subducting slab geometry

Tomographic analysis has revealed a complex picture of the subducting African plate under the Anatolian plate today, with multiple slab windows separating the plate into distinct slabs: the Aegean slab beneath western Turkey, the Cyprus slab beneath Central Anatolia (sometimes separated into western and eastern portions), and the Bitlis slab benearth eastern Turkey (Biryol et al., 2011; Menant et al., 2016; Portner et al., 2018; Kounoudis et al., 2020). While break-off of the Bitlis slab is well established based on the deep, fast anomaly that is unconnected to the subduction zone, a possible break in the Cyprus slab is barely resolvable in tomography, implying that it has either not happened or is very recent. Break-off of the Bitlis slab has been estimated to have occurred during the middle to late Miocene based on the timing of magmatic events (Çolakoğlu & Arehart, 2010; Ekici, 2016; Keskin, 2003, 2007; Keskin et al., 1998; Şengör et al., 2008). An inferred break-off of the Cyprus slab has been suggested sometime from late Miocene to middle Pleistocene based on thermochronology (Karaoğlan, 2016; Karaoğlan et al., 2016), crustal deformation (Kaymakçı et al., 2010), stratigraphy (Cosentino et al., 2012; Radeff et al., 2017; Öğretmen et al., 2018 a-b), and paleotopographic analysis (Schildgen et al., 2014).

3. Materials and methods

Strong variations in Quaternary uplift rates should leave a clear signal in the landscape morphology. In drainage systems of the southern CAP margin, where variations in climate and rock erodibility are relatively minor, major knickpoints along river long profiles and strong changes in river gradient likely reflect variations in uplift rates through time. In our analyses, we focused on rivers that drain from the top of the CAP southern margin directly toward the Mediterranean Sea. We analyzed 1-arc second (~30-m resolution) Shuttle Radar Topography Mission (SRTM) digital topography (downloaded from https://earthexplorer.usgs.gov/) using TopoToolbox (Schwanghart & Scherler, 2014), a MATLAB® toolbox for geomorphological analysis, together with topographic analysis tools from the TAK toolbox (Forte and Whipple, 2019).

3.1 Topographic metrics

We analyzed a slope map derived from the DEM to define the limit of the plateau margin and study variations along its seaward flanks. We also calculated local relief (Stearns, 1967) with a circular sampling window of 2-km radius, which illustrates the characteristic valley-to-ridge relief pattern. We used the topographic metrics and the channel steepness index (see next paragraph) to assess the equilibrium conditions between catchment divides (e.g., Whipple et al., 2016; Scherler and Schwanghart, 2020).

3.2 River profiles

The evolution of a river profile can be described as the change in elevation of a point on a channel through time, which relates to the competition between erosion (E) and uplift (U):

$$\frac{dz(t,x)}{dt} = U(t,x) - E(t,x) \quad (1)$$

Graded river profiles are commonly characterized by an empirical power-law relationship between the local channel slope (*S*) and the upstream drainage area (*A*):

$$S = k_s A^{-\theta} \tag{2}$$

where k_s is the channel steepness index and θ is the concavity index (Hack, 1957, 1960; Flint, 1974). With concave river-channel profiles, θ values are positive, generally ranging between 0.3 and 0.6 (Tucker & Whipple, 2002; Kirby & Whipple, 2012); negative values of θ define convex profiles (Wobus et al., 2006b), which in lithologically homogeneous areas may represent transient profile perturbations induced by an increase in uplift rates (Hoke et al., 2007). We obtained the normalized steepness index values (k_{sn}) for all channels by calculating channel steepness based on a selected reference concavity index (θ_{ref}). The normalized steepness index is a robust measure of relative channel steepness throughout a region and is not sensitive to the exact choice of θ_{ref} (Wobus et al., 2006b). Nevertheless, a representative value of the concavity index can be estimated from the slope of the regression of the logarithm of drainage area and the logarithm of channel slope.

The erosion rate of a bedrock river channel can be described by the equation:

$$E = KA^m S^n \tag{3}$$

where *S* is the local channel gradient (*dz/dt*), *K* is the erosion coefficient related to lithology and climate, and *m* and *n* are two positive coefficients related respectively to basin hydrology and erosion processes in the channel (Howard, 1994; Whipple & Tucker, 1999). θ is defined by the ratio between *m* and *n*.

Equation (3) can be rearranged such that:

$$S = \left(\frac{E}{K}\right)^{\frac{1}{n}} A^{-\theta} \tag{4}$$

Assuming the river profile is in steady-state, meaning the channel erosion rate (*E*) is equal to the uplift rate (*U*), we obtain a new equation that describes how the steepness index (k_s) relates to the uplift rate (Moglen & Bras, 1995; Sklar & Dietrich, 1998):

$$\left(\frac{U}{K}\right)^{\frac{1}{n}} = A^{-\theta}S \quad (5)$$

Equations (4) and (5) describe the relationships among E, U and k_s:

$$\left(\frac{E}{K}\right)^{\frac{1}{n}} = \left(\frac{U}{K}\right)^{\frac{1}{n}} = A^{-\theta}S = k_s \quad (6)$$

If U and K are spatially constant, we can perform an integration of Eq. (5) from a base level x_b to an arbitrary upstream point x of the channel to predict the elevation of the river profile (Perron & Royden, 2013):

$$z(x) = z(x_b) + \left(\frac{U}{KA_0^m}\right)^{\frac{1}{n}}\chi \quad (7)$$

where A_0 is an arbitrary scaling area and χ is an integration of river horizontal coordinates defined by the equation:

$$\chi = \int_{x^b}^{x}\left(\frac{A_0}{A(x')}\right)^{\frac{m}{n}} dx' \quad (8)$$

The new representation of the long-river profile, elevation versus χ, known as the χ plot, is a straight, positively sloping line for concave-upward river channels, while the plot will show breaks-in-slope if knickpoints are present (i.e., separating areas of higher and lower steepness). The slope of the χ plot is proportional to the steepness index, k_s. Excluding influences on the channel slope associated with lithological contrasts and anthropogenic elements (e.g., dams), higher uplift rates are associated with steeper slopes on the χ plot (i.e., greater k_s).

We analysed k_{sn} and χ values of the drainage system to obtain qualitative overviews of uplift histories (based on plots of k_{sn} vs. elevation) and the stability of drainage divides (Whipple et al., 2016). To minimize the effects of lithologic variations on the river profiles, we selected rivers that run over rocks with similar erodibility and marked along the profiles only the knickpoints unrelated to changes in lithology. k_{sn} and χ indexes were calculated for three different θ values (0.35, 0.45, 0.55).

3.3 Uplift histories from linear inversions of river profiles

The response time τ represents the travel time of a perturbation along the river profile from the river outlet (x = 0) to a given point x, and is defined by the equation (Whipple & Tucker, 1999):

$$\tau = \int_0^x \frac{dx'}{K(x')A(x')^m S(x')^{n-1}} \quad (9)$$

τ can account for spatial variations in the erodibility of different rocks because the equation includes path-dependent changes in the erosion coefficient K in the denominator of the integrand. The plot of elevation vs. tau, or τ plot, is similar to the χ plot, but assumes n = 1 and can account for spatial variations in K. The τ plot is the basis for the linear inversion of river profiles to study the rock-uplift/base-level fall history recorded in fluvial topography (Pritchard et al., 2009; Roberts & White, 2010; Goren et al., 2014; Gallen, 2018).

Several studies have employed a spatially uniform erosion coefficient to solve the inverse problem, solving for uplift as a function of space and time on continental scales (Pritchard et al., 2009; Roberts & White, 2010). Although it may be difficult to justifiy the assumption of uniform K over such a large region, this assumption may be safer in smaller areas with rock types of similar erodibility and relatively uniform climate. In our analysis, we assumed constant K and we employed the inverse approach of Goren et al. (2014) and Gallen (2018), which is based on equation (3).

Assuming n = 1 and a block-uplift scenario, the elevation of the river network can be predicted by the equation:

$$z(x) = \int_{-\tau\,(x)}^{0} U(t')dt' \quad (10)$$

where t' is the integration variable, time zero is the present, and the past is represented by negative time. Equation (10) predicts that the present elevation of a given point along a river network $z(x)$ is the integral of the relative uplift rate along the downstream channel points during the past over a duration of $\tau(x)$ and that all tributaries with the same $\tau(x)$ will lie at the same elevation $z(x)$.

Following Gallen (2018), we reconstructed the rock-uplift history from the river network during discrete time intervals using Equation (10), supposing a spatially and temporally constant K. The data organization assumes that N data points of z and τ along the fluvial network that are ordered according to elevation because they share a common uplift history.

By this discretization, Equation (10) can be written for each data point and the equations can be organized in a matrix form:

$$\mathbf{AU}=\mathbf{z} \quad (11)$$

where $\mathbf{A}$ is an $N \times q$ matrix and $\mathbf{z}$ is the elevation.

This is an overdetermined inverse problem, as there are more known data points than unknown parameters. As such, a least squares estimate for $\mathbf{U}$ is used (Tarantola, 1987):

$$\mathbf{U} = \mathbf{U_{pri}} + (\mathbf{A}^T\mathbf{A} + \Gamma^2\mathbf{I})^{-1}\mathbf{A}^T(\mathbf{z} - \mathbf{AU_{pri}}) \quad (12)$$

where Γ is a dampening coefficient that determines the smoothness imposed on the solution, $\mathbf{I}$ is the $q \times q$ identity matrix and $\mathbf{U_{pri}}$ represents the prior guess at the uplift rate. In our river-profile inversions, Γ is automatically calculated by the normalized misfit between the elevation of the river pixels and the predicted elevations with the inferred uplift history (following Goren et al., 2014). Regarding $\mathbf{U_{pri}}$, we set a range of randomly distributed uplift rates between 0 and 4 km/Myr, where the highest value is the highest uplift rate estimated in the area for the late Miocene (Öğretmen et al., 2018a) and selected the best-fit value in a Monte Carlo simulation.

A constant time step ΔT of 50 ky was chosen to determine the number of discrete time intervals in the inversion, as this time step produced good fits to the river profiles without causing numerical instability (Appendix A, Fig. A1). The other assumption implicit in the results of the inversion is that basin divides in the area where river inversion is performed are stable over the duration of the inversion. We performed river-profile inversions for discrete river basins in the study area, selecting stream channels that drain from the top of the margin toward the sea.

The erosion coefficient K was estimated by the ratio between uplift rate and the steepness index inferred from Eq. 6 when n=1. For this estimate, we utilize the uplift rate inferred from marine terraces on the eastern side of the CAP southerm margin by Racano et al. (2020). We first determined the most representative θ of the catchments by the χ-z plot minimization method (Goren et al., 2014) to calculate the normalized steepness index. We then divided the eastern catchments into elevation bands based on the elevation ranges of the marine terraces and extracted the average k_{sn} for each band. Next, we equated K to the slope of the linear relationship between uplift rate and the average k_{sn} for each elevation band estimated by a York regression (York et al., 2004) forced through the axis origin. This approach enabled us to take in account x and y errors and respect the linearity in Eq. 6 that is used to infer K.

We performed sensitivity tests to evaluate the impact of selecting different numbers of rivers within each basin to include in the inversion (Appendix A) and also to evaluate the best-fit erosion coefficient value, K, based on comparisons with the uplift history derived from the marine terraces (Appendix B).

4. Results

4.1 Regional topographic and drainage-system analysis

The CAP southern margin is topped by a high elevation, relatively low-relief surface that slopes gently eastward (Fig. 2a,b,f). The maximum elevation of 2250 m a.s.l. occurs north of Anamur; going toward the east, elevations decrease to 900 m west of Silifke, over a distance of 120 km (Fig. 2e). A major knickzone of the drainage system defines the southern limit of the upper surface (Fig. 2a; Schildgen et al., 2012a).

West of this surface, elevations decrease rapidly to the west over 40 km distance until reaching sea level (Fig. 2e). Overall, the southern flank of the margin is characterized by steep slopes that decrease toward the east (Fig. 2b). West of Aydıncık, high slope values define the limit of the paleosurface atop of the margin. Between Aydıncık and Silifke, the limit is less evident due to the presence of staircase sequences of surfaces that have been recognized as marine terraces (Racano et al., 2020). The west-to-east decrease in slope is mimicked by the local relief (Fig. 2c); toward the west, maximum relief is between 1200 and 1500 m just below the low-relief upper surface, whereas toward the east, it is ca. 600 m. High maximum relief values also characterize the northern edges of the low-relief surface (Fig. 2c).

The topographic differences in slope along the west-east axis of the southern CAP margin are also recorded in river steepness index values (k_{sn}). Like the slope map, the k_{sn} map of the southern flank (Fig. 2d), calculated with a general reference concavity index of 0.45 (similar to values found by McNab et al. (2018) over an even larger area), shows a decrease in values toward the east. Spatial variability in k_{sn} values can result not only from spatial and temporal variations in uplift rate, but also from variations in lithology and climate. Mean annual precipitation varies somewhat across the margin: from ca. 60 to 70 cm in the west to ca. 50 cm in the east (Fig. 2d). Based on empirical observations of the relationship between precipitation and k_{sn} (D'Arcy and Whittaker, 2014), which suggests that k_{sn} scales inversely with the square root of precipitation, the observed difference in rainfall is expected to have a minor (up to 17%) influence on k_{sn} values.

The geology differs more substantially; from basin 1 to basin 4 (Fig. 3a), the bedrock is characterized by Paleozoic and Mesozoic metamorphic rocks (mostly represented by marbles and secondary outcrops of metapelites as schists and phillites) and sedimentary rocks (mostly neritic limestones and clastic units such as sandstones, shales and radiolarites). East of basin 5, there is a predominance of sedimentary rocks, such as neritic limestones and siliciclastic rocks, whereas the Tauride metamorphic bedrock comprises Mesozoic marbles. Shallow-water limestones, calcarenites, marls and conglomerates represent the Miocene and Quaternary marine units that cover the deformed bedrock. (Fig. 3a). Despite this lithologic variability, not all river profiles show significant knickpoints where lithology changes (Fig. 3b-i), but they are marked by a major knickpoint at the edge of the margin-capping paleosurface (Fig. 2a-b). In all the profiles, the shape is broadly similar, showing low gradients in the uppermost portions of the drainage, then a dramatic increase in gradient, then a decrease again at low elevation. The only profile that differs from the others is in Basin 7 (Fig. 3f), which is probably related to the preservation of extensive marine terraces between 1200 and 700 m. a.s.l. (Racano et al., 2020). k_{sn} values downstream from the major knickpoint are highest in the western drainage basins (1 through 4) and decrease toward the east (Fig. 2d). Moreover, the elevations of the major knickpoints follow the same eastward decreasing trend as the elevation of the low-relief paleosurface (Fig. 2e).

To better define the geomorphic signatures of rivers related to the uplift history that affected the area, we focused our analysis on the eight catchments that drain from the top of the margin toward the sea. We considered the main channels for each catchment that flow mostly perpendicular to the coast.

For rivers 1 through 4 (Fig. 4a), the elevations of the knickpoints that delimit the edge of the upper low-relief surface vary from 2200 to 1800 m.a.s.l. River 3 shows another knickpoint located around 400m a.s.l. at a lithological change from Paleozoic metamorphic to Paleozoic/Mesozoic marine rocks. For rivers 5 through 8, the elevations of the major knickpoints decrease from 1400 to 900 m.a.s.l. A well-defined knickpoint around 400 to 450 m.a.s.l. is also present in most of the analysed rivers (excepted for rivers 1, 4 and 6), and is probably related to the development of marine terraces during the Quaternary (Racano et al., 2020).

In several of the χ plots, the major knickpoints identified along the upper portions of the river profiles can be seen as a prominent break in slope (Fig. 4a). In rivers 2, 3, 5, and 7, the signal is less evident, because of the short distance over which rivers cross the upper low-relief surface. The strong increases in k_{sn} suggested by the breaks in slope in the χ plots do not appear to be controlled by changes in lithology alone; river segments downstream from the knickpoints run on different rocks types that do not produce significant changes in the slopes of the plots. For rivers 1 through 5, the χ plots show their steepest slopes between the major knickpoints (at 1800 to 2200 m a.s.l.) and ca. 450 to 500 m a.s.l. The slopes of the χ plots rapidly decrease below 450 to 500 m a.s.l.

For rivers 6 through 8, the highest slopes on the χ plots occur between the major knickpoints (at 1400 to 900 m a.s.l.) and 150 to 300 m a.s.l. Again, the slopes of the χ plots decrease suddenly at lower elevations.

As noted earlier, the slope of the χ-plots correspond to changes in k_{sn} values; this pattern persists regardless of the choice of θ that we applied (Fig. 4a). For each θ value, k_{sn} values increase starting from the major knickpoint on each profile, then reach peak values farther downstream. The elevations at which the highest k_{sn} values occur are different for each river: in rivers 1 and 3, the maximum k_{sn} values occur around 1300 m.a.s.l., whereas in river 2, they occur at an elevation of 1500 m. River 4 shows highest k_{sn} values at around 1200 m; in rivers 5 and 6, the k_{sn} peak is located at an elevation around 800 m. For rivers 7 and 8, the k_{sn} vs. elevation plot is complicated by changes in channel slope related to the marine terraces, but highest values occur at around 500 m and 700 m, respectively. Despite complications in these patterns due to short, low-gradient segments of the rivers, the main trend of the curves shows a hump-shaped distribution of k_{sn} values along the river profiles. The mean k_{sn} value, calculated for a best-fit θ_{ref} of 0.3 (Fig. 4b), estimated for the analyzed drainage system of the selected basins (Fig. 4c) and the elevation where the steepness index reaches the maximum values along the analyzed rivers both generally follow a west-to-east decreasing trend (Fig. 4d).

4.2 Linear inversion verification test and results

Prior to performing the linear inversion, we investigated the relationship between uplift rates and steepness index values (k_{sn}) to evaluate whether there is a linear relationship between these parameters (Fig. 5), which would support the assumption implicit in the inversion that the channel slope exponent, n, equals one. To do so, we compare uplift rates associated with individual marine terraces derived from Racano et al. (2020) with the average k_{sn} calculated for the best-fit θ_{ref} of 0.3 in the elevation bands of the terraces (Fig. 4b). If n=1, vertical movement of steepened sections of the channel will track with vertical movement of the marine terrace (Niemann et al., 2001; Perron & Royden, 2013), and the relationship between k_{sn} and uplift rate will be linear. In Fig. 5b, the York regression between U and the average k_{sn} suggests a K of $3.05*10^{-4}m^{0.4}/yr$ (2σ=$4.06*10^{-5}$). Furthermore, the linear distibution of the points in Fig. 5b supports the assumption of n=1 and justifies our application of the linear inversion.

We first tested the inversion on different sets of rivers within each basin by applying it to basins 5 and 7, where the uplift trend is well documented by the modelling of marine terraces (Racano et al., 2020). Those tests reveal that including all the tributaries in the inversion leads to a large degree of scatter that the inversion does not effectively capture, probably due to some spatial variability in uplift rates within the basin, with peak uplift rates near the coast lower than those in the headwaters (Appendix A). That scatter leads to a poor match to the trunk streams and underestimates of the peak-uplift rate that the main streams experienced. To better capture the magnitude of peak uplift rates recorded by the trunk streams, we performed the linear inversions of only the main channels within 8 selected basins oriented approximately perpendicular to the coast that drain from the paleosurface atop the CAP southern margin to the Mediterranean Sea.

Following the approach of Gallen (2018), we considered a uniform K, and performed the inversion 500 times for each basin with a Monte Carlo simulation, drawing K from a normal distribution with a 1σ of $\pm 2.03*10^{-5}$ based on the standard deviation in the linear fit between k_{sn} versus uplift rate (Fig. 5c).

The inverse modeling results show time-variable rock-uplift trends that can be split into a first phase of decreasing uplift rates followed by a fast and strong uplift pulse occurring sometime between 0.45 and 0.2 Ma. Some differences are evident between the western basins (1, 2, 3 and 4) and the eastern basins (5, 6, 7 and 8). For the western basins, the initial rock-uplift rate (at 0.7 to 0.8 Ma) is estimated at ca. 2 km/Myr and is almost constant until 0.6 Ma (Fig. 6). After 0.6 Ma, all the western rivers record a strong uplift pulse, where the rock uplift drastically increases to between 6.2 and 8.1 km/Myr over a time window of 0.2 to 0.3 Myr, with increasing rates until ca. 0.35 to 0.45 Ma. Subsequently, the uplift rates decrease to between 0.5 and 2 km/Myr at τ = 0. For the eastern basins (5 through 8), during the first half of the inferred history (from 0.8 to 0.5 Ma), the rock-uplift rates and trends are similar to those from the western rivers, but the start of the high-uplift pulse is later, at ca. 0.5 Ma. The peak in rock-uplift rates also occurs later, between 0.2 and 0.3 Ma. The maximum uplift rates of the eastern rivers are lower than the western ones, at ca. 4.5 to 5.9 km/Myr for basins 5, 6 and 8, and ca. 3.2 km/Myr for river 7. The anomalously low peak uplift rate for basin 7 likely relates to the poor fit of the river profiles by the inversion, and in particular the insufficiently steep slopes in the inversion result between ca. 200 and 800 m a.s.l. (Fig. 6). At τ=0, the rock-uplift rates obtained are similar to the western basins (0.5 to 1.7 km/Myr). Changing the value of K applied to all the rivers shifts the time axis of the uplift history, but does not change the general temporal pattern of uplift, nor the spatio-temporal pattern of peak uplift rates occurring earlier in the western basins than in the eastern basins (Appendix B).

5. Discussion

5.1 Uplift history from regional morphology and river-profile inversions

Following the work of Goren et al. (2014), if (1) a linear relationship exists between the steepness index and the uplift rate, (2) uplift rates are uniform in space, and (3) erosion coefficient (K) is uniform in space and unchanging in time, variations in k_{sn} can be related directly to temporal variations in uplift rates. River long profiles that cross the CAP southern margin are marked by major knickpoints, showing a dramatic downstream increase in k_{sn} values, starting near the upper parts of the channel profiles, at around 2000 m.a.s.l. in the west and around 1000 m.a.s.l. in the east. These k_{sn} increases can be related to the strong increase in uplift rates that occurred during the Quaternary based on uplifted middle Pleistocene marine sediments (Öğretmen et al., 2018a). The increase in k_{sn} values subsequently decreases rapidly farther downstream, following a bell-shape trend. If interpreted in terms of an uplift history, these channel profiles indicate a rapid increase in uplift rates followed by a subsequent rapid decrease. These interpretations are qualitatively consistent with the uplift history derived by marine terrace evolution modelling (Racano et al., 2020).

However, our analysis of the morphology of the regional landscape suggests probable west-to-east variations in the uplift history along the southern CAP margin. Mean slope values on hillslopes, the eastward tilt of the paleosurface that caps the margin, the eastward decrease in elevations of the major knickpoints, and mean river steepness index values are all consistent with higher uplift in the west compared to the east. The west-to-east decrease of the steepness index along the plateau margin is independent from the main eroded lithologies (that pass from mainly methamorphic rocks in the west to sedimentary rocks to the east) and shows a trend that is opposite of that expected from the minor decrease in precipitation toward the east (drier regions are expected to show steeper slopes for a given uplift rate and erosion coefficient; D'Arcy & Whittaker, 2014). These observations support our inference that the uplift history is the primary factor that has affected the river profile shapes in the region.

River-profile inversions applied to individual river basins allowed us to obtain quantitative estimates of the Quaternary uplift history. But rather than obtaining a single estimate for the uplift history, the set of rivers spanning the west-east extent of the margin allow us to also investigate possible west-to-east spatial variations in uplift histories.

The first main result regarding the linear inversion regards the estimation of K. The linearity between uplift and k_{sn} justifies the application of the linear inversion model (e.g., Quye-Sawyer et al., 2020) and allows us to estimate the erosion coefficient from the relationship between k_{sn} and uplift (Fig. 5b). Based on our selected K value, our inversion results yield uplift histories that span a time range between 0.8 Ma and the present. However, these results need to be interpreted taking into account the geology of the area, and in particular the Quaternary marine phase that affected the eastern side of the CAP southern margin until the middle Pleistocene. The biostratigraphical analysis performed by Öğretmen et al. (2018a,b) atop the plateau margin reveals that the area experienced marine deposition until 0.47 Ma. The results of the river-profile inversion are inconsistent with the age of the marine sediments, because they include a history of the drainage system older that the end of marine sedimentation. We shade out that region in Fig. 6 to indicate that that portion should not be considered. However, the western side of the plateau margin lacks Quaternary marine sediments, and the preserved coastline on top of the eastern plateau margin (Öğretmen et al., 2018a; Racano et al., 2020) suggests that the western area remained above sea-level during the Quaternary. In this case, the reconstructed rock-uplift history could be considered reliable for the whole period, assuming that the drainage divides remained stable (discussed below). Considering that a continental paleolandscape existed prior to the Quaternary uplift pulse, the low-gradient upper portion of the river profiles may reliably approximate the pre-uplift, relict landscape.

The inferred uplift histories from the western and eastern basins show a bell-shaped trend for the middle to late Pleistocene. However, the peak uplift rates differ in timing and magnitude between the western and the eastern sides of the plateau margin. In the west, the start of the increased uplift rates occurs around 0.7 Ma, and the peak rates occur around 0.4 Ma, reaching up to ca. 5.0 to 7.9 km/Myr (Fig. 6a, c). In the east, the uplift pulse starts later, around 0.4 Ma, and the peak rates occur at ca. 0.25 Ma, with maximum rock-uplift rates of 3.0 to 5.7 km/Myr (or 4.5 to 5.8 km/Myr, excluding Basin 7) (Fig. 6b, d). These inferred uplift histories from the river-profile inversions are similar to the mean uplift history obtained by modelling marine terraces from the CAP southern margin, which are located within the drainage basins of rivers 5, 6, 7, and 8 (Racano et al., 2020). For those eastern basins, the marine terrace uplift history lies within the uncertainty bounds of the rock-uplift history obtained by river-profile inversion (Fig. 6d). We argue that there is no circularity in this comparison, even though the erosion coefficient K is calibrated from the marine terrace uplift record, because the calibration only determines the relationship between local channel gradients and uplift rate, not the shape of the uplift curve. This agreement between the uplift history derived from marine-terrace modeling and that derived from our river-profile inversion provides additional support for our initial inference that the slope exponent, n, is indistinguishable from 1.

Our results showing that western basins record earlier peak uplift times and higher peak uplift rates (Fig. 7) are robust; even for K values lower or higher than $3.05*10^{-4}$ $m^{0.4}$/yr, applied uniformly along the plateau margin, the inversion change the absolute timing of uplift but do not change the relative timing between western and eastern sides (Appendix B), supporting our inference that the uplift pulse affected first the western side of the plateau margin and moved eastward through time. However, differences in lithology could result in spatial variations in *K* between the western (1 through 4) and eastern (5 through 8) drainage basins. Unfortunately, no useful constraints are available to estimate independently the erosion coefficient for the western basins. Nevertheless, if the western basins had a lower erosion coefficient, *K*, compared to the eastern basins, as one may expect given the greater prevalence of metamorphic rocks, the timing of uplift in the west would be even older than we have estimated. Hence, the potential spatial variations in *K* that one might expect based on the mapped geology will not affect our interpretation that the peak-uplift pulse proceded from west to east through time.

The dependency of the response time on the erosion coefficient *K* (Eq. 9) is also illustrated by comparing our results to those of McNab et al. (2018). Although that study performed river-profile inversions over a much larger region, their results from the southern margin of the CAP show similarities with the results here, with uplift starting earlier in the western basins compared to the eastern basins (Fig. 6a-f in McNab et al., 2018). Other important differences between that study and ours is that McNab et al. (2018) used the late Miocene marine sediments atop the southern CAP margin, rather than the more recently described middle Pleistocene marine sediments (Öğretmen et al., 2018a) and marine terraces (Racano et al., 2020), to perform their calibration of *K*, and also that our "local" study, compared with a larger regional study like McNab et al. (2018), allowed us to show the west-to-east propagation of the uplift by addressing the effects of likely spatial differences in *K*, divide and shoreline migrations. This difference results in a much lower *K* value in the McNab et al. (2018) inversions, and a much longer response time compared to our analysis. For example, rapid uplift of the western basins from McNab et al. (2018) starts at ca. 6 to 5 Ma, whereas in our inversion, the start is at ca. 0.4 to 0.5 Ma.

5.2. Effects of changes in channel length on river-profile inversions

The formation of marine terraces during uplift implies a seaward migration of the shoreline through time (Fig. 5a). However, the calculation of the integral τ assumes a steady-state position of the basin outlet through time. The effect of shoreline migration would be to lengthen the river profile, causing the uplift history inferred by the τ plot for the upstream reaches to shift further back in time compared to a scenario with no shoreline migration. However, the good agreement of the surface uplift trend inferred by marine terrace analysis (Racano et al., 2020) and the rock-uplift trend obtained by river-profile inversion in the same region as the marine terraces suggests that the effects of shoreline migration on the inversion results are negligible. This finding could imply that any shoreline migration that occurred was minor, which seems reasonable considering the steep slopes in the region. Considering that the coast becomes even steeper going westward, we can assume that the magnitude of shoreline migration was even lower (and hence, less important) in the west. However, if shoreline migration had the effect of making the timing of apparent uplift look older, then the timing in the east has been made to look artifically older more so than in the west. Thus, any effect of shoreline migration does not alter the conclusion that the uplift pulse was earlier in the west than in the east.

Shifts in the drainage divides could also change the channel length and affect the results of the river-profile inversions. Specifically, lengthening at the upstream end will cause newly added portions of the drainage network to have high τ values, which we may then incorrectly interpret as reflecting the earliest portion of the uplift history. Also, the added drainage area will decrease τ values downstream, causing the overall uplift history to shift to more recent times. For the western basins in particular, hillslope values, local relief, and k_{sn} values suggest that drainage divides between the Göksu basin (on the low-relief upper surface) and the south-draining catchments (basins 1 through 4) are unstable, with divides that should have a tendency to migrate toward the Göksu basin. However, similar to our argument concerning shoreline migration, the contribution of divide migration is unlikely to be important for our results because basin lengthening over the past ca. 0.5 Myr would likely be minor along the steep plateau margins. An increase in area in the west would decrease τ for a given point on the river, making the uplift timing apparently younger than it should be. If divide migration was significant, since it only seems likely to have affected the western basins, the timing of uplift in those basins could be older than it appears in our inversions. The result would still be consistent with west-to-east propagation of the uplift pulse.

5.3 Spatial variations in CAP southern margin uplift and uplift mechanism

The first evident geomorphological feature of the CAP southern margin is the eastward tilt of the present-day plateau-margin topography. Our river-profile analysis reveals that this tilt can be explained through differential uplift of the western and eastern sides of the margin during the middle Pleistocene uplift phase. Based on our river-profile inversions, the western side of the margin experienced a peak in uplift rates 100 to 200 kyr earlier than the eastern side, and the mean uplift rate is faster (mean of ca. 6.1 km/Myr on the western side versus 4.3 km/Myr on the eastern side, Fig. 7).

Different mechanisms have been invoked to explain the topography that has developed at the CAP southern margin, including slab break-off (Cosentino et al., 2012; Schildgen et al, 2012a-b, 2014; Öğretmen et al., 2018a), removal of lithospheric mantle and crustal thickening (Meijers et al., 2018), continental collision (McPhee & van Hinsbergen, 2019) and thermal-viscous deformation of the crust (Fernàndez-Blanco et al., 2019; 2020). However, mechanisms like crustal underplating or thermal-viscous deformation (Meijers et al., 2018, Fernàndez-Blanco et al., 2019; 2020) estimate maximum uplift rates between 0.4 and 0.7 km/Myr (Mejers et al., 2018; Fernàndez-Blanco et al., 2019; 2020). As a result, they cannot account for the very rapid uplift rates, with peaks exceeding 3 km/Myr, that have occurred during the middle Pleistocene, which are supported by biostratigrpahic results on uplifted marine seidments (Öğretmen et al., 2018a), marine terrace modelling (Racano et al., 2020), and the river-inversion results presented here. Following numerical simulations by Duretz & Gerya (2013) and Magni et al. (2017), the mechanism that best fits with the uplift history and landscape evolution at the CAP southern margin is the break-off of the subducting slab (Fig. 8). Geodynamic models suggest that a slab break-off event can trigger a rapid increase in uplift rates over very short time windows, on the order of 100 ky, with peak uplift rates reaching up to 7 to 9 km/Myr (Duretz & Gerya, 2013).

Other characteristics of the subducting slabs, such as slab tears orthogonal to the trench, may have influenced the uplift history of the CAP southern margin. Low velocity anomalies between the Aegean and Cyprus slabs (Biryol et al., 2011; Bakırcı et al., 2012; Salaün et al., 2012; Portner et al., 2018; Kounoudis et al., 2020), differences in GPS-derived velocity vectors (Barka & Reilinger, 1997) and earthquake focal mechanisms (Özbakır et al., 2013) have been used to suggest a tear with upwelling asthenosphere between the Cyprus and Aegean slabs. If this slab tear is responsible for the west-to-east differences in uplift histories along the CAP southern margin, then the orthogonal tear is likely a recent (i.e., middle Pleistocene) feature of the subducting slab, which was followed shortly by break-off of the Cyprus slab. Alternatively, the west-to-east variation in the uplift history may result from a west-to-east propagation of slab tearing within the Cyprus slab. In their recent tomography, Portner et al. (2018) show a tear in the eastern portion of the Cyprus slab, beneath our study region, but no tear in the western portion of the slab (to the west of our westernmost analyzed drainage basin) (Fig. 8). A west-to-east propagation direction for a break-off in the Cyprus slab would thus imply that the Cyprus slab is cut by a tear in the trench-orthogonal direction, as was inferred in the tomography by Biryol et al. (2011), and could be corroborated by the existance of the Paphos transform fault, which separates the trenches associated with each portion of the slab.

6. Conclusions

Qualitative analysis of the southern CAP margin morphology combined with linear inversions of river profiles draining the southern flank of the margin reveal that the Quaternary uplift pulse responsible for km-scale growth of the plateau margin was variable in space and time. An overall eastward tilt of the margin is defined by the eastward dip of the margin-capping planar surface, a west-to-east decrease in the elevation of the knickpoints that mark the edge of the surface, and a west-to-east decrease in topographic gradients and river steepness values. From a qualitative river-profile analyses, we argue that along-channel variations in k_{sn} values indicate that uplift rates increased and then decreased through time. Quantitatively, our linear inversion of river profiles yielded uplift histories that are comparable with the uplift history obtained by terrace-evolution modelling of marine terraces along the eastern sector of the southern CAP margin (Racano et al., 2020). The river-profile inversion also revealed differences in the timing and rates of the Quaternary uplift pulse between the western and the eastern sides of the CAP southern margin: on the western side, the estimated age of the uplift peak is around 0.4 Ma, with instantaneous rock uplift rates of up to 6.1 km/Myr, whereas on the eastern side, the peak rock-uplift is recorded at 0.25 Ma with rates of 4.3 km/Myr. The differences in uplift histories are consistent with the current eastward tilt of the plateau margin. Together, the temporal pattern of the rock-uplift rates and the obtained magnitude of uplift rates are consistent with crustal rebound following slab break-off in very recent times, with lateral variations in the uplift history resulting from eastward migration of a tear in the Cyprus slab and/or enhanced mantle upwelling between the Cyprus and Aegean slabs prior to break-off of the Cyprus slab.

Appendix A: Sensitivity of linear inversion results to time steps and the number of channels included

The setup of the river-profile inversion with regards to the time-step and number of tributary channels to include has been principally tested for Basin 5, which is mostly oriented N-S and located on the eastern side of the CAP southern margin, where the Quaternary uplit trend has been estimated by the modeling of marine terrace evolution (Racano et al., 2020). In Gallen (2018), the base-level fall rate of the southern Apalachian drainage system is derived from a Monte Carlo routine with a loop of 1000 simulations, and estimating the $\mathbf{U_{pri}}$ (Eq. 12) by Equation (13). Here, we instead set a range of uplift rates to use in the MonteCarlo routine between 0 (no uplift) and the average post-Middle Pleistocene uplift estimated for the CAP southern margin based on uplifted marine sediments (4000 m/Myr, Öğretmen et al., 2018a).

We first estimated the time-steps for the inversion on the main trunk stream of the Basin 5. For 6 different time steps (Fig. A1), we compared the empirical τ plots (*τ versus river elevations)* and best-fit τ plots, where the elevation is calculated multiplying the inferred uplift for the matrix A (Eq. 11), to find the time-step that generates the lowest percentage of error (0.05 Myr) without creating excessive scatter in the inferred uplift history.

We performed the linear inversion on Basin 5 using various sets of streams within the basin to assess the effect of inverting a single trunk stream versus the full set of tributaries. We applied a Monte Carlo routine of 500 simulations on the trunk stream alone in Fig. A2a, then also for each channel that drains from the paleosurface on the top of the margin toward the sea (Fig. A2b), and finally for all the basin streams with a minimum drainage area of 1 km^2 (Fig. A2c). The three different analyses show similar results, identifying the rock-uplift peak at around 0.25 Ma. However, the inversion results for the main trunk stream alone (Fig. A2a) shows peak uplift rates that are higher than the other two analyses (Fig. A2b,c), which could be related to some spatial variability in uplift. For example, if the peak uplift rates near the outlet were lower than the peak uplift rate near the headwaters, tributaries that only drain the lower reaches of the catchment will force the inversion of all streams to find a lower average peak uplift rate.

We tested the effects of inverting different numbers of streams also for Basin 7, which is located on the eastern side of the CAP southern margin, but has a drainage-basin shape mostly elongated along the east-west direction. The analysis (Fig. A3) shows strong differences in the inferred uplift history results when including more tributaries in the inversion. For the first inversion (Fig. A3a) performed along a N-S oriented stream channel, the uplift-rate trend is concordant with our qualitative analysis and with the linear inversion results derived from the Basin 5 streams. Similar results are also obtained in Fig. A3b, where the first half of the river path follows an eastward direction, parallel to the tilting direction of the plateau margin. In Fig. A3c, we selected the rivers that drain from the top of the margin with a perpendicular-to-coast path. The Quaternary uplift peak is smoother than the first two results and becomes even more smooth when the inversion is performed for all the channels

(Fig. A3b). Considering the inversion made for the whole drainage system with a time step of 0.05 Myr, the rock-uplift trend shows two peaks with a strong drop in uplift rate at the timing of the maximum uplift inferred in Racano et al. (2020) (Fig. A3c). Considering that in the river inversion, knickpoints are interpreted as changes in uplift rate, the presence of well preserved low-gradient levels related to marine terraces appear to 'contaminate' the analysis. This possibility would imply that a time step of 0.05 Myr is a too highly resolved to exclude the effects of Quaternary sea-level variations in the Basin 7 inversion for the whole catchment. By increasing the time step to 0.75 Myr (e), the splitting of the uplift peak is nearly eliminated, and the uplift trend looks similar to the inversions made for the selected main N-S streams.

These results illustrate that using only the main trunk stream in the inversion results in a peak-uplift pulse that is shorter in duration and higher in magnitude compared to using all of the tributary channels in the inversion. Regardless of our choice, peak uplift rates reach several km/Myr, and the duration is limited to a few 100 kyr. Considering that our choice has little impact on the final results, we performed the linear inversions for all the main streams that drain from the top of the margin toward the sea. The final setup of the inversions is reported in Table A1.

Appendix B: Erodibility test for the western side of the CAP southern margin

For different rock types under different climate conditions, values of K can show significant variations, from 10^{-7} to 10^{-3} $m^{0.1}$/yr (e.g., Gallen et al., 2013; Miller et al., 2013; Gallen, 2018; Li et al., 2020; Ma et al., 2020). In these papers the erosion parameter is usually calculated, assuming n=1, by the ratio between the erosion rate and the average k_{sn} of the basin, inferring K from the linear regression of the k_{sn} versus erosion rate plot (e.g., Gallen et al., 2013; Miller et al., 2013; Gallen, 2018; Li et al., 2020; Ma et al., 2020) or the ratio between k_{sn} and erosion rates (e.g., Kirkpatrick et al., 2020).

Following Eq. 6, we used the uplift instead of the erosion rate to infer the erosion parameter from the history of the marine terrace evolution (Racano et al., 2020). We used both the k_{sn} /uplift ratio and the linear regression between k_{sn} and uplift rate to estimate the erosion parameter and verify the goodness of the result (Fig. B1). To calculate the ratio between k_{sn} and uplift (Fig. B1b), we first divided the eastern catchments of the CAP southern margin that drain from the top of the plateau to the sea and where marine terraces are mapped, into elevation bands, where elevation ranges are defined by the outer edges of marine terraces. When then divided the average k_{sn} of each band with the uplift at the age of the relate marine terrace. The result is a mean K of $3.27*10^{-4}m^{0.4}/yr$ with a standard deviation of $9.1*10^{-5}$ (Fig. B1c).

Calculating the average k_{sn} for each elevation band on the eastern side of the plateau margin (Fig. B1d), we can see as the relation between k_{sn} and uplift is almost linear, suggesting that the assumption of n=1 can be applied for the study area and allowing the estimation of K from the linear regression of the plotted points. We applied the York regression method (York et al., 2014), which considers errors both in x and y, to estimate the slope of the linear fit in the k_{sn} versus uplift plot. The resulting K is $3.74*10^{-4}m^{0.4}/yr$ (standard deviation of $4.68*10^{-5}$, R^2 of 0.98), which is fairly close to the average k_{sn} /uplift ratio. However, this linear regression does not intercept the plot origin at [0;0], neither the axis origin is comprised in the 2σ bounds. Considering that the linear regression of the k_{sn} versus uplift plot is based on Eq. 6, the intersection with the axis origin is a necessary condition for estimating K. We performed a second test that forced the York regression through the axis origin, obtaining a K of $3.05*10^{-4}m^{0.4}/yr$ (standard deviation of $4.06*10^{-5}$, R^2 of 0.92), which is much closer to the value obtained from the k_{sn} /uplift ratios and respects the linearity of Eq. 6.

Comparing the three estimated values for the erosion parameter in the linear inversion for the Basin 5 main trunk (Fig. B2a), the results are almost the same, showing small differences in uplift history (from 0.9 to 0.7 Myr) and maximum uplift rates (from 6.8 to 7.4 km/Myr), but providing a timing of the middle Pleistocene uplift pulse very similar to the one estimated in Racano et al. (2020) (Fig. B2b). Considering that the K of $3.05*10^{-4}m^{0.4}/yr$ respects the linearity relation between k_{sn} and uplift of Eq. 6 and has the lower standard deviation, we used this erosion parameter value in our river-profile linear inversions.

If we apply a reference concavity index (θ_{ref}) of 0.45 for the k_{sn} estimation, as is commonly assumed in river inversion studies (e.g., Gallen, 2018; McNab et al., 2018; Li et al., 2020; Ma et al., 2020), and we calculate K as before (Fig. B3a,b,c), the resulting estimations are somewhat similar to the ones made for a θ_{ref} of 0.3 (Fig. B1) but the order of magnitude decreases, passing from 10^{-4} to 10^{-5}. Performing the inversion with this new K and θ_{ref} on the main trunk channel in Basin 5 (Fig. B3d) results in an inferred uplift trend similar to the one shown in Fig. B2, however, the uplift history and the timing of the uplift peak shift to significantly younger ages (from 0.2 to 0.1 Myr), without overlapping the uplift peak inferred from marine terrace modeling. This test illustrates how, despite similarities in the resulting uplift trend for different θ_{ref} values, accurate definition of the most representative concavity index in the estimation of K and in linear inversions is critical for inferring an accurate uplift history.

For the western side of the CAP southern margin, we tested the impact of several K values on the linear inversions of the main trunk stream of Basin 1 (Fig. B4a), the westernmost analyzed basin. The geology of the basin is mostly characterized by Paleozoic limestones and marbles and Mesozoic limestones (Fig. 3). The first test (Fig. B4b) was made by varying the exponential term of the erosion coefficient between 10^{-5} and 10^{-3} $m^{0.4}$/yr. We found the lowest uncertainties for the rock-uplift estimations and rock-uplift histories that are consistent with the geological and stratigraphic history known for the region by using K=10^{-4} $m^{0.4}$/yr. Specifically, we know that the area experienced two different uplift phases, the first in the late Messinian and the second during the middle Pleistocene, and that until 0.47 Ma, the eastern basins of the CAP southern margin (basins 5 through 8) experienced marine sedimentation (e.g., Cosentino et al., 2012; Schildgen et al., 2014; Radeff et al., 2017; Öğretmen et al., 2018a).

Progressively increasing K shifts the uplift peak toward younger ages (Fig. B4c). When using K values of $4*10^{-4}$ $m^{0.4}$/yr to $5*10^{-4}$ $m^{0.4}$/yr, the peak uplift overlaps in time with the peak uplift inferred from marine terrace modeling in Racano et al. (2020). However, the western side of the CAP southern margin is characterized by higher steepness values than the area of the marine terraces

(Basin 5) (Figs. 2, 3). For that reason, detailed comparisons with the marine-terrace modeling results are best done with Basin 5.

Acknowledgments

The grant to Dipartimento di Scienze, Università degli Studi Roma Tre (MIUR-Italy Dipartimenti di Eccellenza, articolo 1, commi 314 – 337 legge 232/2016) is gratefully acknowledged for support of S.R. We gratefully acknowledge also the Helmholtz-Zentrum Potsdam – Deutsches GeoForschungsZentrum (GFZ) – Section 4.6 (Geomorphology) for the financial support given to complete the research. Data used in the paper include digital elevation data from the Shuttle Radar Topography Mission, available for free download at https://earthexplorer.usgs.gov. The code used for river-profile inversions will be uploaded and archived to Zenodo during revisions.

References

Aksu, A. E., Calon, T. J., Hall, J., Mansfield, S., & Yaşar, D. (2005). The Cilicia–Adana basin complex, Eastern Mediterranean: Neogene evolution of an active fore-arc basin in an obliquely convergent margin. *Marine Geology*, *221*(1), 121–159. https://doi.org/10.1016/j.margeo.2005.03.011

Aksu, A. E., Walsh-Kennedy, S., Hall, J., Hiscott, R. N., Yaltırak, C., Akhun, S. D., & Çifçi, G. (2014). The Pliocene–Quaternary tectonic evolution of the Cilicia and Adana basins, eastern Mediterranean: Special reference to the development of the Kozan Fault zone. *Tectonophysics*, *622*, 22–43. https://doi.org/10.1016/j.tecto.2014.03.025

Bakırcı, T., Yoshizawa, K., & Özer, M. F. (2012). Three-dimensional S-wave structure of the upper mantle beneath Turkey from surface wave tomography: 3-D upper-mantle structure beneath Turkey. *Geophysical Journal International*, *190*(2), 1058–1076. https://doi.org/10.1111/j.1365-246X.2012.05526.x

Ballato, P., Uba, C. E., Landgraf, A., Strecker, M. R., Sudo, M., Stockli, D. F., et al. (2011). Arabia-Eurasia continental collision: Insights from late Tertiary foreland-basin evolution in the Alborz Mountains, northern Iran. *Geological Society of America Bulletin*, *123*(1–2), 106–131. https://doi.org/10.1130/B30091.1

Barka, A. A., & Kadinsky-Cade, K. (1988). Strike-slip fault geometry in Turkey and its influence on earthquake activity. *Tectonics*, *7*(3), 663–684. https://doi.org/10.1029/TC007i003p00663

Bartol, J., & Govers, R. (2014). A single cause for uplift of the Central and Eastern Anatolian plateau? *Tectonophysics*, *637*, 116–136. https://doi.org/10.1016/j.tecto.2014.10.002

Berndt, C., Yıldırım, C., Çiner, A., Strecker, M. R., Ertunç, G., Sarıkaya, M. A., et al. (2018). Quaternary uplift of the northern margin of the Central Anatolian Plateau: New OSL dates of fluvial and delta-terrace deposits of the Kızılırmak River, Black Sea coast, Turkey. *Quaternary Science Reviews*, *201*, 446–469. https://doi.org/10.1016/j.quascirev.2018.10.029

Biryol, C., Beck, S. L., Zandt, G., & Özacar, A. A. (2011). Segmented African lithosphere beneath the Anatolian region inferred from teleseismic P-wave tomography: Segmented lithosphere beneath Anatolia. *Geophysical Journal International*, *184*(3), 1037–1057. https://doi.org/10.1111/j.1365-246X.2010.04910.x

Burke, K., & Sengör, C. (1986). Tectonic escape in the evolution of the continental crust. In M. Barazangi & L. Brown (Eds.), *Geodynamics Series*, *14*, 41–53. Washington, D. C.: American Geophysical Union. https://doi.org/10.1029/GD014p0041

Büyüksaraç, A., Jordanova, D., Ateş, A., & Karloukovski, V. (2005). Interpretation of the Gravity and Magnetic Anomalies of the Cappadocia Region, Central Turkey. *Pure and Applied Geophysics*, *162*(11), 2197–2213. https://doi.org/10.1007/s00024-005-2712-9

Çiner, A., Doğan, U., Yıldırım, C., Akçar, N., Ivy-Ochs, S., Alfimov, V., et al. (2015). Quaternary uplift rates of the Central Anatolian Plateau, Turkey: insights from cosmogenic isochron-burial nuclide dating of the Kızılırmak River terraces. *Quaternary Science Reviews*, *107*, 81–97. https://doi.org/10.1016/j.quascirev.2014.10.007

Çolakoğlu, A. R., & Arehart, G. B. (2010). The petrogenesis of Sarıçimen (Çaldıran-Van) quartz monzodiorite: Implication for initiation of magmatism (Late Medial Miocene) in the east Anatolian collision zone, Turkey. *Lithos*, *119*(3), 607–620. https://doi.org/10.1016/j.lithos.2010.08.014

Cosentino, D., Schildgen, T. F., Cipollari, P., Faranda, C., Gliozzi, E., Hudackova, N., et al. (2012). Late Miocene surface uplift of the southern margin of the Central Anatolian Plateau, Central Taurides, Turkey. *Geological Society of America Bulletin*, *124*(1–2), 133–145. https://doi.org/10.1130/B30466.1

D'Arcy, M., & Whittaker, A. C. (2014). Geomorphic constraints on landscape sensitivity to climate in tectonically active areas. *Geomorphology*, *204*, 366–381. https://doi.org/10.1016/j.geomorph.2013.08.019

Dewey, J. F., & Şengör, A. M. C. (1979). Aegean and surrounding regions: Complex multiplate and continuum tectonics in a convergent zone. *Geological Society of America Bulletin*, *90*(1), 84. https://doi.org/10.1130/0016-7606(1979)90<84:AASRCM>2.0.CO;2

Duretz, T., & Gerya, T. V. (2013). Slab detachment during continental collision: Influence of crustal rheology and interaction with lithospheric delamination. *Tectonophysics*, *602*, 124–140. https://doi.org/10.1016/j.tecto.2012.12.024

Ehlers, T. A., & Poulsen, C. J. (2009). Influence of Andean uplift on climate and paleoaltimetry estimates. *Earth and Planetary Science Letters*, *281*(3–4), 238–248. https://doi.org/10.1016/j.epsl.2009.02.026

Ekici, T. (2016). Collision-related slab break-off volcanism in the Eastern Anatolia, Kepez volcanic complex (Turkey). *Geodinamica Acta*, *28*(3), 223–239. https://doi.org/10.1080/09853111.2015.1121796

Faccenna, C., Bellier, O., Martinod, J., Piromallo, C., & Regard, V. (2006). Slab detachment beneath eastern Anatolia: A possible cause for the formation of the North Anatolian fault. *Earth and Planetary Science Letters*, *242*(1–2), 85–97. https://doi.org/10.1016/j.epsl.2005.11.046

Fernández-Blanco, D., Bertotti, G., Aksu, A., & Hall, J. (2019). Monoclinal flexure of an orogenic plateau margin during subduction, south Turkey. *Basin Research*, *31*(4), 709–727.

https://doi.org/10.1111/bre.12341

Fernández-Blanco, D., Mannu, U., Bertotti, G., & Willett, S. D. (2020). Forearc high uplift by lower crustal flow during growth of the Cyprus-Anatolian margin. *Earth and Planetary Science Letters*, *544*, 116–314. https://doi.org/10.1016/j.epsl.2020.116314

Flint, J. J. (1974). Stream gradient as a function of order, magnitude, and discharge. *Water Resources Research*, *10*(5), 969–973. https://doi.org/10.1029/WR010i005p00969

Forte, A. M., & Whipple, K. X. (2019) Short communication: The Topographic Analysis Kit (TAK) for TopoToolbox. *Earth Surface Dynamics*, 7, 87-95, https://doi.org/10.5194/esurf-7-87-2019

Fox, M., Goren, L., May, D. A., & Willett, S. D. (2014). Inversion of fluvial channels for paleorock uplift rates in Taiwan. *Journal of Geophysical Research: Earth Surface*, *119*(9), 1853–1875. https://doi.org/10.1002/2014JF003196

Fox, M., Leith, K., Bodin, T., Balco, G., & Shuster, D. L. (2015). Rate of fluvial incision in the Central Alps constrained through joint inversion of detrital 10Be and thermochronometric data. *Earth and Planetary Science Letters*, *411*, 27–36. https://doi.org/10.1016/j.epsl.2014.11.038

Gans, C. R., Beck, S. L., Zandt, G., Biryol, C. B., & Ozacar, A. A. (2009). Detecting the limit of slab break-off in central Turkey: new high-resolution Pn tomography results. *Geophysical Journal International, 179(3)*, 1566–1572. https://doi.org/10.1111/j.1365-246X.2009.04389.x

Gallen, S.F., Wegmann, K.W., & Bohnenstiehl, D.R. (2013). Miocene rejuvenation of to-pographic relief in the southern Appalachians. *GSA Today, 23*, 4–11. https://doi .org /10 .1130 /GSATG163A.1.

Gallen, S. F. (2018). Lithologic controls on landscape dynamics and aquatic species evolution in post-orogenic mountains. *Earth and Planetary Science Letters*, *493*, 150–160. https://doi.org/10.1016/j.epsl.2018.04.029

Göğüş, O. H., Pysklywec, R. N., Şengör, A. M. C., & Gün, E. (2017). Drip tectonics and the enigmatic uplift of the Central Anatolian Plateau. *Nature Communications*, *8*(1), 1538. https://doi.org/10.1038/s41467-017-01611-3

Goren, L., Fox, M., & Willett, S. D. (2014). Tectonics from fluvial topography using formal linear inversion: Theory and applications to the Inyo Mountains, California. *Journal of Geophysical Research: Earth Surface*, *119*(8), 1651–1681. https://doi.org/10.1002/2014JF003079

Gregory-Wodzicki, K. M. (2000). Uplift history of the Central and Northern Andes: A review. *GSA Bulletin*, *112*(7), 1091–1105. https://doi.org/10.1130/0016-7606(2000)112<1091:UHOTCA>2.0.CO;2

Güneş, P., Aksu, A. E., & Hall, J. (2018). Internal seismic stratigraphy of the Messinian evaporites across the northern sector of the eastern Mediterranean Sea. *Marine and Petroleum Geology*, *91*, 297–320. https://doi.org/10.1016/j.marpetgeo.2018.01.016

Hack, J. T. (1957). Studies of longitudinal stream profiles in Virginia and Maryland. *Shorter Contrib. Gen. Geol*, (294), 45–97.

Hack, J. T. (1960). Interpretation of erosional topography in humid temperate regions. *American Journal of Science*, *Bradley Volume*(258), 80–97.

Harris, N. (2006). The elevation history of the Tibetan Plateau and its implications for the Asian monsoon. *Palaeogeography, Palaeoclimatology, Palaeoecology*, *241*(1), 4–15. https://doi.org/10.1016/j.palaeo.2006.07.009

Hartley, A. (2003). Andean uplift and climate change. *Journal of the Geological Society*, *160*(1), 7–10. https://doi.org/10.1144/0016-764902-083

Hoke, G. D., Isacks, B. L., Jordan, T. E., Blanco, N., Tomlinson, A. J., & Ramezani, J. (2007). Geomorphic evidence for post-10 Ma uplift of the western flank of the central Andes 18°30′-22°S. *Tectonics*, *26*(5). https://doi.org/10.1029/2006TC002082Howard, A. D. (1994). A detachment-limited model of drainage basin evolution. *Water Resources Research*, *30*(7), 2261–2285. https://doi.org/10.1029/94WR00757

Howard, A. D., & Kerby, G. (1983). Channel changes in badlands. *GSA Bulletin*, *94*(6), 739–752. https://doi.org/10.1130/0016-7606(1983)94<739:CCIB>2.0.CO;2Karaoğlan, F. (2016). Tracking the uplift of the Bolkar Mountains (south-central Turkey): evidence from apatite fission track thermochronology. *Turkish Journal of Earth Sciences*, *25*(1), 64–80.

Karaoğlan, F., Parlak, O., Hejl, E., Neubauer, F., & Klötzli, U. (2016). The temporal evolution of the active margin along the Southeast Anatolian Orogenic Belt (SE Turkey): Evidence from U–Pb, Ar–Ar and fission track chronology. *Gondwana Research*, *33*, 190–208. https://doi.org/10.1016/j.gr.2015.12.011

Kaymakci, N., Inceöz, M., Ertepinar, P., & Koç, A. (2010). Late Cretaceous to Recent kinematics of SE Anatolia (Turkey). *Geological Society, London, Special Publications*, *340*(1), 409–435. https://doi.org/10.1144/SP340.18

Keskin, M., Pearce, J. A., & Mitchell, J. G. (1998). Volcano-stratigraphy and geochemistry of collision-related volcanism on the Erzurum–Kars Plateau, northeastern Turkey. *Journal of Volcanology and Geothermal Research*, *85*(1), 355–404. https://doi.org/10.1016/S0377-0273(98)00063-8

Keskin, M. (2003). Magma generation by slab steepening and breakoff beneath a subduction-accretion complex: An alternative model for collision-related volcanism in Eastern Anatolia, Turkey: Model for collision-related volcanism. *Geophysical Research Letters*, *30*(24). https://doi.org/10.1029/2003GL018019

Keskin, M. (2007). Eastern Anatolia: A hotspot in a collision zone without a mantle plume. In *Special Paper 430: Plates, Plumes and Planetary Processes* (Vol. 430, pp. 693–722). Geological Society of America. https://doi.org/10.1130/2007.2430(32)

Ketin, I. (1948). Über die tektonisch-mechanischen Folgerungen aus den großen anatolischen Erdbeben des letzten Dezenniums. *Geologische Rundschau*, *36–36*(1), 77–83. https://doi.org/10.1007/BF01791916

Kirby, E., & Whipple, K. (2001). Quantifying differential rock-uplift rates via stream profile analysis. *Geology*, *29*(5), 415. https://doi.org/10.1130/0091-7613(2001)029<0415:QDRURV>2.0.CO;2

Kirby, E., & Whipple, K. X. (2012). Expression of active tectonics in erosional landscapes. *Journal of Structural Geology*, *44*, 54–75. https://doi.org/10.1016/j.jsg.2012.07.009

Kirkpatrick, H. M., Moon, S., Yin, A., & Harrison, T. M. (2020). Impact of fault damage on eastern

Tibet topography. *Geology*. https://doi.org/10.1130/G48179.1

Kounoudis, R., Bastow, I. D., Ogden, C. S., Goes, S., Jenkins, J., Grant, B., & Braham, C. (2020). Seismic Tomographic Imaging of the Eastern Mediterranean Mantle: Implications for Terminal-Stage Subduction, the Uplift of Anatolia, and the Development of the North Anatolian Fault. *Geochemistry, Geophysics, Geosystems*, *21*(7). https://doi.org/10.1029/2020GC009009

Lenters, J. D., & Cook, K. H. (1997). On the Origin of the Bolivian High and Related Circulation Features of the South American Climate. *Journal of the Atmospheric Sciences*, *54*(5), 656–678. https://doi.org/10.1175/1520-0469(1997)054<0656:OTOOTB>2.0.CO;2

Li, X., Zhang, H., Wang, Y., Zhao, X., Ma, Z., Liu, K., & Ma, Y. (2020). Inversion of bedrock channel profiles in the Daqing Shan in Inner Mongolia, northern China: Implications for late Cenozoic tectonic history in the Hetao Basin and the Yellow River evolution. *Tectonophysics*, *790*, 228558. https://doi.org/10.1016/j.tecto.2020.228558

Lüdecke, T., Mikes, T., Rojay, F. B., Cosca, M. A., & Mulch, A. (2013). Stable isotope-based reconstruction of Oligo-Miocene paleoenvironment and paleohydrology of Central Anatolian lake basins (Turkey). *Turkish Journal of Earth Sciences 22*(5)*,* 793-819. https://doi.org/10.3906/yer-1207-11

Ma, Z., Zhang, H., Wang, Y., Tao, Y., & Li, X. (2020). Inversion of Dadu River Bedrock Channels for the Late Cenozoic Uplift History of the Eastern Tibetan Plateau. *Geophysical Research Letters*, *47*(4). https://doi.org/10.1029/2019GL086882Magni, V., Allen, M. B., van Hunen, J., & Bouilhol, P. (2017). Continental underplating after slab break-off. *Earth and Planetary Science Letters*, *474*, 59–67. https://doi.org/10.1016/j.epsl.2017.06.017

McKenzie, D. (1978). Active tectonics of the Alpine–Himalayan belt: the Aegean Sea and surrounding regions. *Geophysical Journal International*, *55*(1), 217–254. https://doi.org/10.1111/j.1365-246X.1978.tb04759.x

McNab, F., Ball, P. W., Hoggard, M. J., & White, N. J. (2018). Neogene Uplift and Magmatism of Anatolia: Insights From Drainage Analysis and Basaltic Geochemistry. *Geochemistry,* *Geophysics, Geosystems*, *19*(1), 175–213. https://doi.org/10.1002/2017GC007251

McPhee, P. J., & van Hinsbergen, D. J. J. (2019). Tectonic reconstruction of Cyprus reveals Late Miocene continental collision of Africa and Anatolia. *Gondwana Research*, *68*, 158–173. https://doi.org/10.1016/j.gr.2018.10.015

McPhee, P. J., Altıner, D., & van Hinsbergen, D. J. J. (2018). First Balanced Cross Section Across the Taurides Fold-Thrust Belt: Geological Constraints on the Subduction History of the Antalya Slab in Southern Anatolia. *Tectonics*, *37*(10), 3738–3759. https://doi.org/10.1029/2017TC004893

Meijers, M. J. M., Brocard, G. Y., Cosca, M. A., Lüdecke, T., Teyssier, C., Whitney, D. L., & Mulch, A. (2018). Rapid late Miocene surface uplift of the Central Anatolian Plateau margin. *Earth and Planetary Science Letters*, *497*, 29–41. https://doi.org/10.1016/j.epsl.2018.05.040

Menant, A., Sternai, P., Jolivet, L., Guillou-Frottier, L., & Gerya, T. (2016). 3D numerical modeling of mantle flow, crustal dynamics and magma genesis associated with slab roll-back and tearing: The eastern Mediterranean case. *Earth and Planetary Science Letters*, *442*, 93–107. https://doi.org/10.1016/j.epsl.2016.03.002

Miller, S.R., Sak, P.B., Kirby, E., & Bierman, P.R. (2013). Neogene rejuvenation of central Appalachian topography: evidence for differential rock uplift from stream pro-files and erosion rates. *Earth and Planetary Science Letters, 369–370*, 1–12. https://doi .org /10 .1016 /j .epsl .2013 .04 .007.

Moglen, G. E., & Bras, R. L. (1995). The Effect of Spatial Heterogeneities on Geomorphic Expression in a Model of Basin Evolution. *Water Resources Research*, *31*(10), 2613–2623. https://doi.org/10.1029/95WR02036

Molnar, P., England, P., & Martinod, J. (1993). Mantle dynamics, uplift of the Tibetan Plateau, and the Indian Monsoon. *Reviews of Geophysics*, *31*(4), 357. https://doi.org/10.1029/93RG02030

Niemann, J. D., Gasparini, N. M., Tucker, G. E., & Bras, R. L. (2001). A quantitative evaluation of Playfair's law and its use in testing long-term stream erosion models. *Earth Surface Processes and Landforms*, *26*(12), 1317–1332. https://doi.org/10.1002/esp.272

Öğretmen, N., Cipollari, P., Frezza, V., Faranda, C., Karanika, K., Gliozzi, E., et al. (2018a). Evidence for 1.5 km of Uplift of the Central Anatolian Plateau's Southern Margin in the Last 450 kyr and Implications for Its Multiphased Uplift History. *Tectonics*, *37*(1), 359–390. https://doi.org/10.1002/2017tc004805

Öğretmen, N., Frezza, V., Hudáčková, N., Gliozzi, E., Cipollari, P., Faranda, C., et al. (2018b). Early Pleistocene (Calabrian) marine bottom oxygenation and palaeoclimate at the southern margin of the Central Anatolian Plateau. *Italian Journal of Geosciences*, *137*(3), 425–464. https://doi.org/10.3301/ijg.2018.19

Okay, A. I., Zattin, M., & Cavazza, W. (2010). Apatite fission-track data for the Miocene Arabia-Eurasia collision. *Geology*, *38*(1), 35–38. https://doi.org/10.1130/G30234.1

Perron, J. T., & Royden, L. (2013). An integral approach to bedrock river profile analysis: Integral approach to river profile analysis. *Earth Surface Processes and Landforms*, *38*(6), 570–576. https://doi.org/10.1002/esp.3302

Portner, D. E., Delph, J. R., Biryol, C. B., Beck, S. L., Zandt, G., Özacar, A. A., et al. (2018). Subduction termination through progressive slab deformation across Eastern Mediterranean subduction zones from updated P-wave tomography beneath Anatolia. *Geosphere*, *14*(3), 907–925. https://doi.org/10.1130/GES01617.1

Pritchard, D., Roberts, G. G., White, N. J., & Richardson, C. N. (2009). Uplift histories from river profiles. *Geophysical Research Letters*, *36*(24). https://doi.org/10.1029/2009GL040928

Quye-Sawyer, J., Whittaker, A. C., & Roberts, G. G. (2020). Calibrating fluvial erosion laws and quantifying river response to faulting in Sardinia, Italy. *Geomorphology*, *370*, 107388. https://doi.org/10.1016/j.geomorph.2020.107388

Racano, S., Jara-Muñoz, J., Cosentino, D., & Melnick, D. (2020). Variable Quaternary uplift along the southern margin of the Central Anatolian Plateau inferred from modeling marine terrace sequences. *Tectonics*, 39, e2019TC005921. Accepted Author Manuscript. https://doi.org/10.1029/2019TC005921

Radeff, G., Cosentino, D., Cipollari, P., Schildgen, T. F., Iadanza, A., Strecker, M., et al. (2016).

Stratigraphic architecture of the upper Messinian deposits of the Adana Basin (Southern Turkey): implications for the Messinian salinity crisis and the Taurus petroleum system. *Italian Journal of Geosciences*, *135*(3), 408–424. https://doi.org/10.3301/ijg.2015.18

Radeff, G., Schildgen, T. F., Cosentino, D., Strecker, M. R., Cipollari, P., Darbaş, G., & Gürbüz, K. (2017). Sedimentary evidence for late Messinian uplift of the SE margin of the Central Anatolian Plateau: Adana Basin, southern Turkey. *Basin Research*, *29*, 488–514. https://doi.org/10.1111/bre.12159

Reilinger, R. E., McClusky, S. C., Oral, M. B., King, R. W., Toksoz, M. N., Barka, A. A., et al. (1997). Global Positioning System measurements of present-day crustal movements in the Arabia-Africa-Eurasia plate collision zone. *Journal of Geophysical Research: Solid Earth*, *102*(B5), 9983–9999. https://doi.org/10.1029/96JB03736

Roberts, G. G., & White, N. (2010). Estimating uplift rate histories from river profiles using African examples. *Journal of Geophysical Research*, *115*(B2). https://doi.org/10.1029/2009JB006692

Roberts, G. G., Paul, J. D., White, N., & Winterbourne, J. (2012a). Temporal and spatial evolution of dynamic support from river profiles: A framework for Madagascar: DYNAMIC SUPPORT OF MADAGASCAR. *Geochemistry, Geophysics, Geosystems*, *13*(4). https://doi.org/10.1029/2012GC004040

Roberts, G. G., White, N. J., Martin-Brandis, G. L., & Crosby, A. G. (2012b). An uplift history of the Colorado Plateau and its surroundings from inverse modeling of longitudinal river profiles. *Tectonics*, *31*(4). https://doi.org/10.1029/2012TC003107

Ruddiman, W. F., & Kutzbach, J. E. (1989). Forcing of late Cenozoic northern hemisphere climate by plateau uplift in southern Asia and the American west. *Journal of Geophysical Research*, *94*(D15), 18409. https://doi.org/10.1029/JD094iD15p18409

Salaün, G., Pedersen, H. A., Paul, A., Farra, V., Karabulut, H., Hatzfeld, D., et al. (2012). High-resolution surface wave tomography beneath the Aegean-Anatolia region: constraints on upper-mantle structure: Tomography of Aegea-Anatolia upper mantle. *Geophysical Journal International*, *190*(1), 406–420. https://doi.org/10.1111/j.1365-246X.2012.05483.x

Scherler, D., & Schwanghart, W. (2020). Drainage divide networks – Part 2: Response to perturbations. *Earth Surface Dynamics*, 8, 261-274, https://doi.org/10.5194/esurf-8-261-2020

Schildgen, T. F., Cosentino, D., Bookhagen, B., Niedermann, S., Yıldırım, C., Echtler, H., et al. (2012a). Multi-phased uplift of the southern margin of the Central Anatolian plateau, Turkey: A record of tectonic and upper mantle processes. *Earth and Planetary Science Letters*, *317–318*, 85–95. https://doi.org/10.1016/j.epsl.2011.12.003

Schildgen, T. F., Cosentino, D., Caruso, A., Buchwaldt, R., Yıldırım, C., Bowring, S. A., et al. (2012b). Surface expression of eastern Mediterranean slab dynamics: Neogene topographic and structural evolution of the southwest margin of the Central Anatolian Plateau, Turkey. *Tectonics*, *31*(2). https://doi.org/10.1029/2011TC003021

Schildgen, T. F., Yıldırım, C., Cosentino, D., & Strecker, M. R. (2014). Linking slab break-off, Hellenic trench retreat, and uplift of the Central and Eastern Anatolian plateaus. *Earth-Science Reviews*, *128*, 147–168. https://doi.org/10.1016/j.earscirev.2013.11.006

Schwanghart, W., & Scherler, D. (2014). Short Communication: TopoToolbox 2 – MATLAB-based software for topographic analysis and modeling in Earth surface sciences. *Earth Surface Dynamics*, *2*(1), 1–7. https://doi.org/10.5194/esurf-2-1-2014

Şengör, A.M. Celâl, Özeren, M. S., Keskin, M., Sakınç, M., Özbakır, A. D., & Kayan, İ. (2008). Eastern Turkish high plateau as a small Turkic-type orogen: Implications for post-collisional crust-forming processes in Turkic-type orogens. *Earth-Science Reviews*, *90*(1), 1–48. https://doi.org/10.1016/j.earscirev.2008.05.002

Şengör, A.M.C. (1980). Türkiye'nin Neotektoniginin Esasları (Essentials of the Turkish Neotectonics). *Conference Series*, *2*, 40.

Şengör, A.M.C., Gorür, N., & Şaroğlu, F. (1985). Strike-slip faulting and basin related formation in zones of tectonic escape: Turkey as a case study. In: Biddle, K.T., Christie-Blick, N. (Eds.), Strike-slip Deformation, Basin Formation and Sedimentation. *Society of Economic Paleontologists and Mineralogists Special Publication*, *37*, 227–440.

Sklar, L., & Dietrich, W. E. (1998). River longitudinal profiles and bedrock incision models: Stream power and the influence of sediment supply. In J. Tinkler & E. Wohl (Eds.), *Geophysical Monograph Series* (Vol. 107, pp. 237–260). Washington, D. C.: American Geophysical Union. https://doi.org/10.1029/GM107p0237

Stearns, R. G. (1967). Warping of the Western Highland Rim Peneplain in Tennessee by Ground-Water Sapping. *Geological Society of America Bulletin*, *78*(9), 1111. https://doi.org/10.1130/0016-7606(1967)78[1111:WOTWHR]2.0.CO;2

Strecker, M. R., Alonso, R. N., Bookhagen, B., Carrapa, B., Hilley, G. E., Sobel, E. R., & Trauth, M. H. (2007). Tectonics and Climate of the Southern Central Andes. *Annual Review of Earth and Planetary Sciences*, *35*(1), 747–787. https://doi.org/10.1146/annurev.earth.35.031306.140158

Tarantola, A. (1988). Inverse Problem Theory. Methods for Data Fitting and Model Parameter Estimation. *Geophysical Journal International*, *94*(1), 167–168. https://doi.org/10.1111/j.1365-246X.1988.tb03436.x

Tucker, G. E., & Whipple, K. X. (2002). Topographic outcomes predicted by stream erosion models: Sensitivity analysis and intermodel comparison. *Journal of Geophysical Research: Solid Earth*, *107*(B9), ETG 1–1–ETG 1–16. https://doi.org/10.1029/2001JB000162

Tucker, G. E., & Slingerland, R. (1996). Predicting sediment flux from fold and thrust belts. *Basin Research*, *8*(3), 329–349. https://doi.org/10.1046/j.1365-2117.1996.00238.x

Whipple, K. X., & Tucker, G. E. (1999). Dynamics of the stream-power river incision model: Implications for height limits of mountain ranges, landscape response timescales, and research needs. *Journal of Geophysical Research: Solid Earth*, *104*(B8), 17661–17674. https://doi.org/10.1029/1999JB900120

Whipple, K. X., Kirby, E., & Brocklehurst, S. H. (1999). Geomorphic limits to climate-induced increases in topographic relief. *Nature*, *401*(6748), 39–43. https://doi.org/10.1038/43375

Whipple, K. X., Forte, A. M., DiBiase, R. A., Gasparini, N. M., & Ouimet, W. B. (2016). Timescales of landscape response to divide migration and drainage capture: Implications for the role of divide mobility in landscape evolution. *Journal of Geophysical Research: Earth Surface*, *122*(1), 248–273. https://doi.org/10.1002/2016JF003973Wobus, C. W., Crosby, B. T., &

Whipple, K. X. (2006a). Hanging valleys in fluvial systems: Controls on occurrence and implications for landscape evolution. *Journal of Geophysical Research*, *111*(F2). https://doi.org/10.1029/2005JF000406

Wobus, C., Whipple, K. X., Kirby, E., Snyder, N., Johnson, J., Spyropolou, K., et al. (2006b). Tectonics from topography: Procedures, promise, and pitfalls. In *Special Paper 398: Tectonics, Climate, and Landscape Evolution* (Vol. 398, pp. 55–74). Geological Society of America. https://doi.org/10.1130/2006.2398(04)

Yildirim, C., Melnick, D., Ballato, P., Schildgen, T. F., Echtler, H., Erginal, A. E., et al. (2013a). Differential uplift along the northern margin of the Central Anatolian Plateau: inferences from marine terraces. *Quaternary Science Reviews*, *81*, 12–28. https://doi.org/10.1016/j.quascirev.2013.09.011

Yildirim, C., Schildgen, T. F., Echtler, H., Melnick, D., Bookhagen, B., Çiner, A., et al. (2013b). Tectonic implications of fluvial incision and pediment deformation at the northern margin of the Central Anatolian Plateau based on multiple cosmogenic nuclides: Uplift rate in the Central Pontides. *Tectonics*, *32*(5), 1107–1120. https://doi.org/10.1002/tect.20066

York, D., Evensen, N. M., Martínez, M. L., & De Basabe Delgado, J. (2004). Unified equations for the slope, intercept, and standard errors of the best straight line. *American Journal of Physics*, *72*(3), 367–375. https://doi.org/10.1119/1.1632486

Zhisheng, A., Kutzbach, J. E., Prell, W. L., & Porter, S. C. (2001). Evolution of Asian monsoons and phased uplift of the Himalaya–Tibetan plateau since Late Miocene times. *Nature*, *411*(6833), 62–66. https://doi.org/10.1038/35075035

Figure Captions

Figure 1: Regional simplified tectonic boundaries and topography of the Anatolian Microplate (modified from Cosentino et al., 2012 & Yildirim et al., 2013). *CAP*: Central Anatolian Plateau; *EAP*: Eastern Anatolian Plateau; *WAP*: Western Anatolian Province; *NAF*: North Anatolian Fault; *EAF*: East Anatolian Fault; *DST*: Death Sea Transform Fault; *CA*: Cyprus Arc; *PT*: Paphos

Transform; *AS*: Antalya Slab; *ALF*: Amos-Larnaka Fault; *KA*: Kyrenia Range; *AKF*: Aksu-Kyrenia Fault; *KkF:* Kirkkavak Fault; *SAF*: Silifke-Anamur Fault; *EF:* Ecemiş Fault; *KzF*: Kozan Fault; *MKF*: Misis-Kyrenia Fault; *ACB*: Adana-Cilicia Basin. Red box shows region of Figure 2.

Figure 2: Topographic metrics at the southern margin of the Central Anatolian Plateau. a) topographic map, drainage basins analyzed for river-profile inversions, major knickpoints and trace of the swath profile (shown in f); b) slope map with margin of the plateau limit marked; c) local-relief map calculated with a circular sampling window of 2000 m of radius, and analyzed basins; d) k_{sn} map, with values calculated with a reference concavity value of 0.45 and contours of mean annual rainfall; e) swath profile and main knickpoint evelations.

Figure 3: Geology and analyzed river basins. a) Geological map of the CAP southern margin. Geology simplified from 1:500,000 scale geologic maps (Şenel, 2002; Ulu,2002): 1) Quaternary continental deposits; 2) Quaternary marine units (marls and calcarenites); 3) Miocene marine units (mostly neritic and shallow water limestones passing to marls in the area of Silifke); 4) Miocene clastic units (mostly conlomerates and breccias); 5) Mesozoic continental units (clastic rocks); 6) Mesozoic marine units (neritic limestones); 7) Mesozoic ophiolitic melange; 8) Mesozoic metamorphic units (marble and secondary metaflysch); 9)Triassic volcanic rocks (basalts); 10) Paleozoic marine units (carbonates and flysch); 11) Paleozoic metamorphic units (mainly foliated rocks and marbles); 12) Undifferentiated pre-Cambrian metasedimentary rocks; b – i) river profiles of the analyzed basins colored by the geology.

Figure 4: a) Qualitative analysis of the main trunks of the selected basins, illustrating a) river long profiles colored by lithology (legend in Fig. 3), χ plots, and k_{sn} vs. elevation plots for different θ values; b) estimation of the best concavity index for the rivers in the southern margin of the CAP; c)

distribution of k_{sn} values for the whole drainage system in the selected basins (Fig. 2d); d) k_{sn} peak elevations of selected rivers.

Figure 5: a) Map of marine terraces and Quaternary marine units atop the CAP southern margin (from Öğretmen et al., 2018a; Racano et al., 2020) and elevation-bands used for the estimation of the average k_{sn} at the level of marine terraces and shoreline migration rate estimated for the last 450 ka; b) K estimation from the York regression forced through the origin of the average k_{sn} from the marine terrace elevation ranges versus U.

Figure 6: Linear inversions of the main streams of each selected basin with channel heads on the top of the margin. The river-profile inversion has been performed for a time-step of 0.05 Myr (see Appendix A) and running a MonteCarlo routine of 500 simulations for each set of stream channels. The black curves in τ-plots and the uplift history (inversion results) display the best-fit results, and the red curves show the one standard deviation ($\pm 1\sigma$) of the MonteCarlo simulation.

Figure 7: Rock-uplift histories for selected rivers (a-b), mean rock-uplift trend and standard deviation ($\pm 1\sigma$) estimated for the western (c) and eastern (d) sides of the study area. Blue line in (d) shows the surface uplift-trend estimated by Racano et al. (2020) on the eastern side of the CAP southern margin based on marine-terrace modelling. The gray box indicates the marine deposition phase in the eastern side of the plateau (Öğretmen et al., 2018a-b), where the uplift history derived from the inversion should be ignored.

Figure 8: Schematic illustration of upwelling asthenosphere through a lithospheric slab break and tear (modified from Schildgen et al., 2012b; geometry of slabs from Portner et al. 2018), with map above

showing regions of low Pn-wave velocities in red (Gans et al., 2009) and the differential rock-uplift rates related to the Quaternary topographic growth of the CAP southern margin.

Table A1: setup parameters for the river linear inversion in the CAP southern margin

Figure A1: Linear inversion of the main trunk stream of Basin 5 using different time steps; a) basin map and main trunk stream; b) main trunk stream long-river profile; c) empirical and best-fit τ-plots for different time steps; d) inversion results for the selected time-step; e) best-fit estimated time step.

Figure A2: Linear inversion results for Basin 5 based on a time step of 0.05 Myr performed for the main trunk stream (a), the selected rivers with channel-heads on the top of the margin (b) and for the whole drainage system extracted with a minimum drainage area of $1km^2$ (c).

Figure A3: Linear inversion results for Basin 7 based on a time step of 0.05 Myr performed for a N-S trunk stream (a), the main trunk stream (b), the selected rivers with channel-heads on the top of the margin that drain perpendicular to the coast (c), and for the whole drainage system, with a time step of 0.05 (d) and 0.075 (e) Myr, extracted with a minimum drainage area of $1km^2$.

Figure B1: a) ratio between the average k_{sn} (using a θ_{ref} of 0.3) at the level of marine terraces for each seaward catchment on the eastern side of the CAP southern margin and the uplift rate, dot color gradient indicates the relative West-East position of the elevation band in each basin; b) mean of the ratio between k_{sn} and uplift for each elevation band, the green solid line indicates the K_{mean}, dashed lines the standard deviation; c) K estimation from the York regression forced (red) and unforced through the origin (blue) of the average k_{sn} from the marine terrace elevation ranges vs the uplift, solid lines indicate the mean linear regression, dashed lines the standard deviation. In plots b and c, the color of the points is related to the elevation ranges in Fig. 5.

Figure B2: Basin 5 main trunk (a) and river linear inversion (b) performed with the erosion coefficients estimated in Fig. B1 from the mean of the k_{sn}/uplift ratio (green), the York fit forced through the origin (red) and the unforced York fit (blue), and comparison with the uplift history inferred from marine terrace modeling by Racano et al. (2020).

Figure B3: Erosion parameter estimation for θ_{ref}=0.45 by (a-b) the mean ratio between the average k_{sn} at the level of marine terraces and the uplift, (c) the York regression forced (red) and unforced through the origin (blue), and (d) inversion made on the main trunk of Basin 5 for the 3 estimated K. Legend of plots (a),(b) and (c) is in Fig. B1 caption.

Figure B4: Tests of different *K* values for the trunk channel of Basin 1 on the western side of the CAP southern margin: a) Basin 1 main trunk and river profile; b) river-profile inversion test for *K* between 10^{-5} to 10^{-3} $m^{0.1}$/yr (with increments of one order-of-magnitude) and best-fit result (blue *K*); b) river inversion test for *K* between 10^{-4} to $5*10^{-4}$ $m^{0.1}$/yr, and comparison with the uplift inferred from marine terrace modeling by Racano et al. (2020). In all the inversions the 2 σ is arbitrary set to one order-of-magnitude less than *K*.

Figure 1.

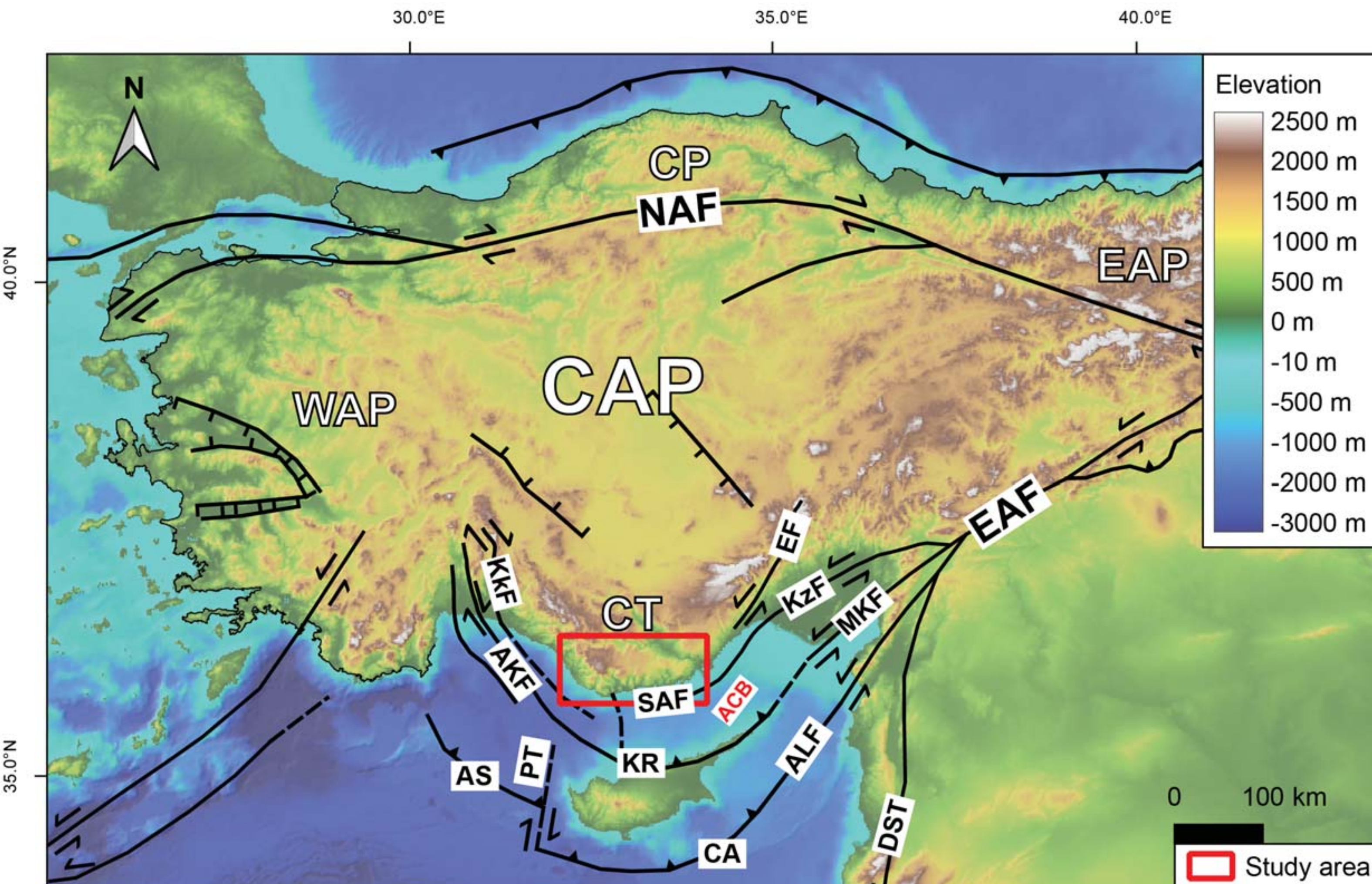

30.0°E
35.0°E
40.0°E
40.0°N
35.0°N
N
Elevation
2500 m
2000 m
1500 m
1000 m
500 m
0 m
-10 m
-500 m
-1000 m
-2000 m
-3000 m
CP
NAF
EAP
CAP
WAP
EAF
EF
KkF
KzF
MKF
CT
AKF
SAF
ACB
ALF
AS
PT
KR
DST
CA
0
100 km
Study area

Figure 2.

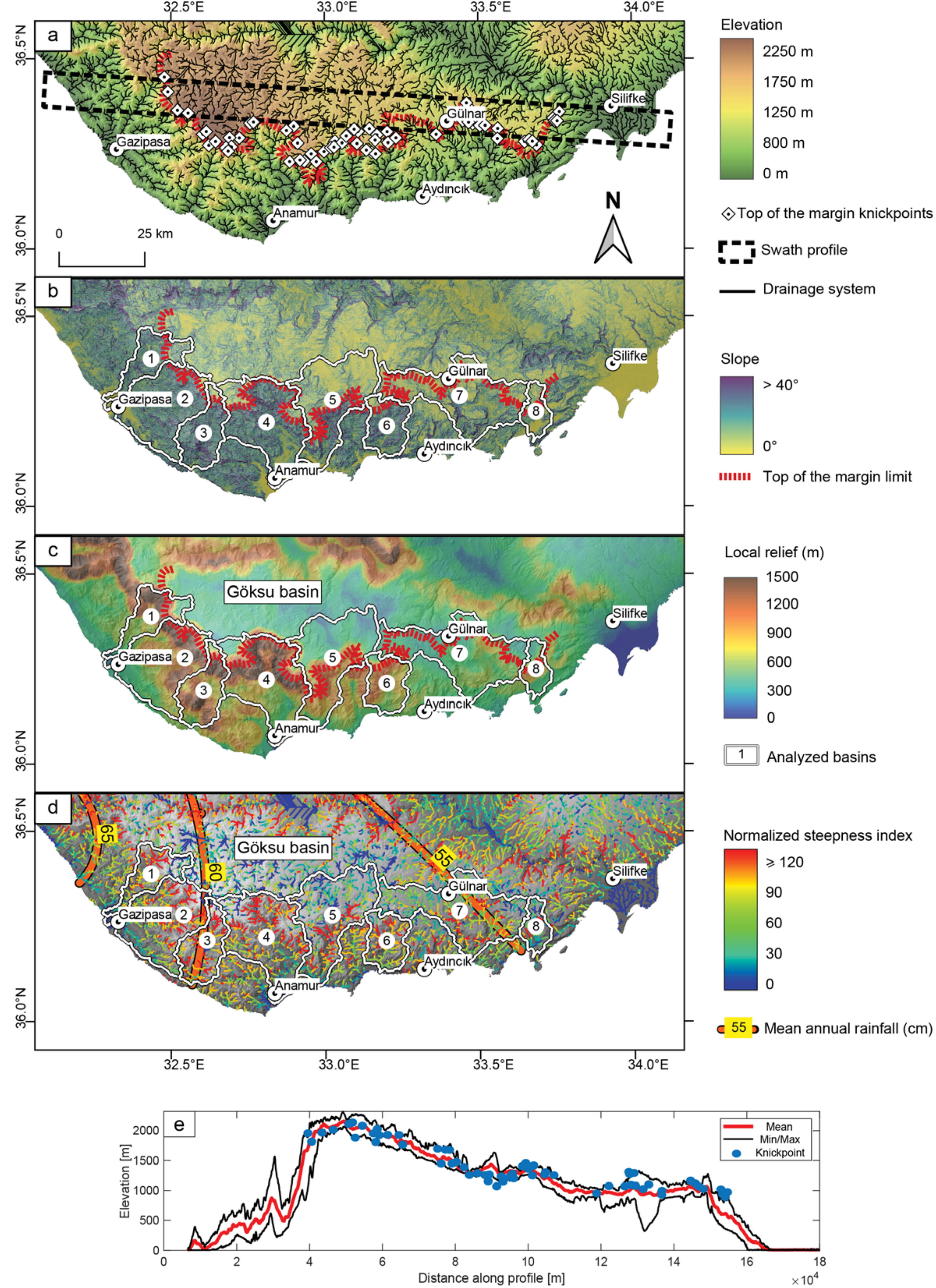

a
b
c
d
e
32.5°E
33.0°E
33.5°E
34.0°E
36.5°N
36.0°N
Elevation
2250 m
1750 m
1250 m
800 m
0 m
Top of the margin knickpoints
Swath profile
Drainage system
Slope
> 40°
0°
Top of the margin limit
Local relief (m)
1500
1200
900
600
300
0
Analyzed basins
Normalized steepness index
⩾ 120
90
60
30
0
Mean annual rainfall (cm)
Gazipasa
Anamur
Aydıncık
Gülnar
Silifke
Göksu basin
0
25 km
N
65
60
55
Elevation [m]
Distance along profile [m]
Mean
Min/Max
Knickpoint
×10^4

Figure 3.

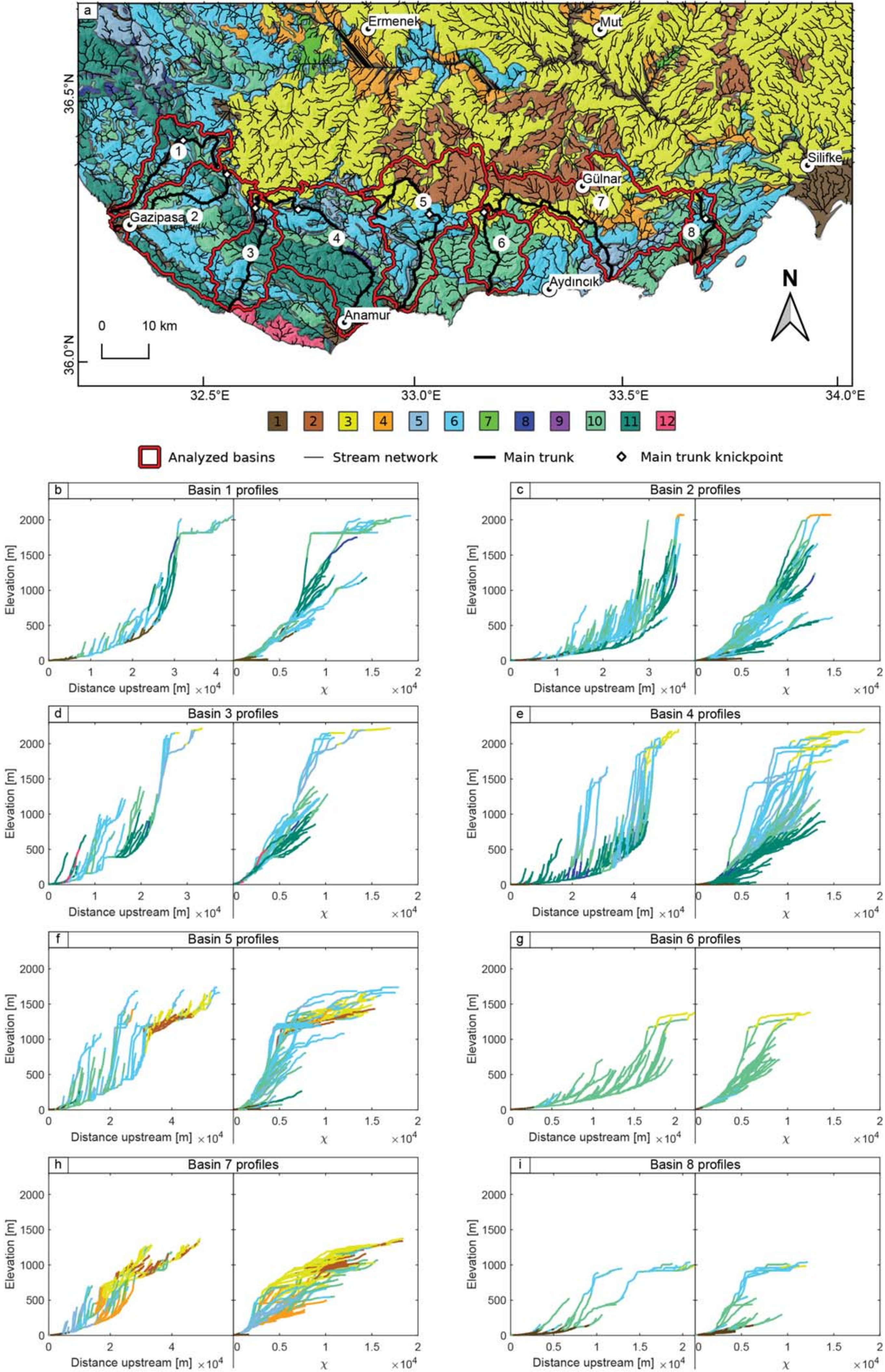

a
Ermenek
Mut
Silifke
Gülnar
Gazipasa
Anamur
Aydıncık
36.5°N
36.0°N
32.5°E
33.0°E
33.5°E
34.0°E
0
10 km
N
1 2 3 4 5 6 7 8 9 10 11 12
Analyzed basins
Stream network
Main trunk
Main trunk knickpoint
b Basin 1 profiles
c Basin 2 profiles
d Basin 3 profiles
e Basin 4 profiles
f Basin 5 profiles
g Basin 6 profiles
h Basin 7 profiles
i Basin 8 profiles
Elevation [m]
Distance upstream [m] $\times 10^4$
χ $\times 10^4$

Figure 4.

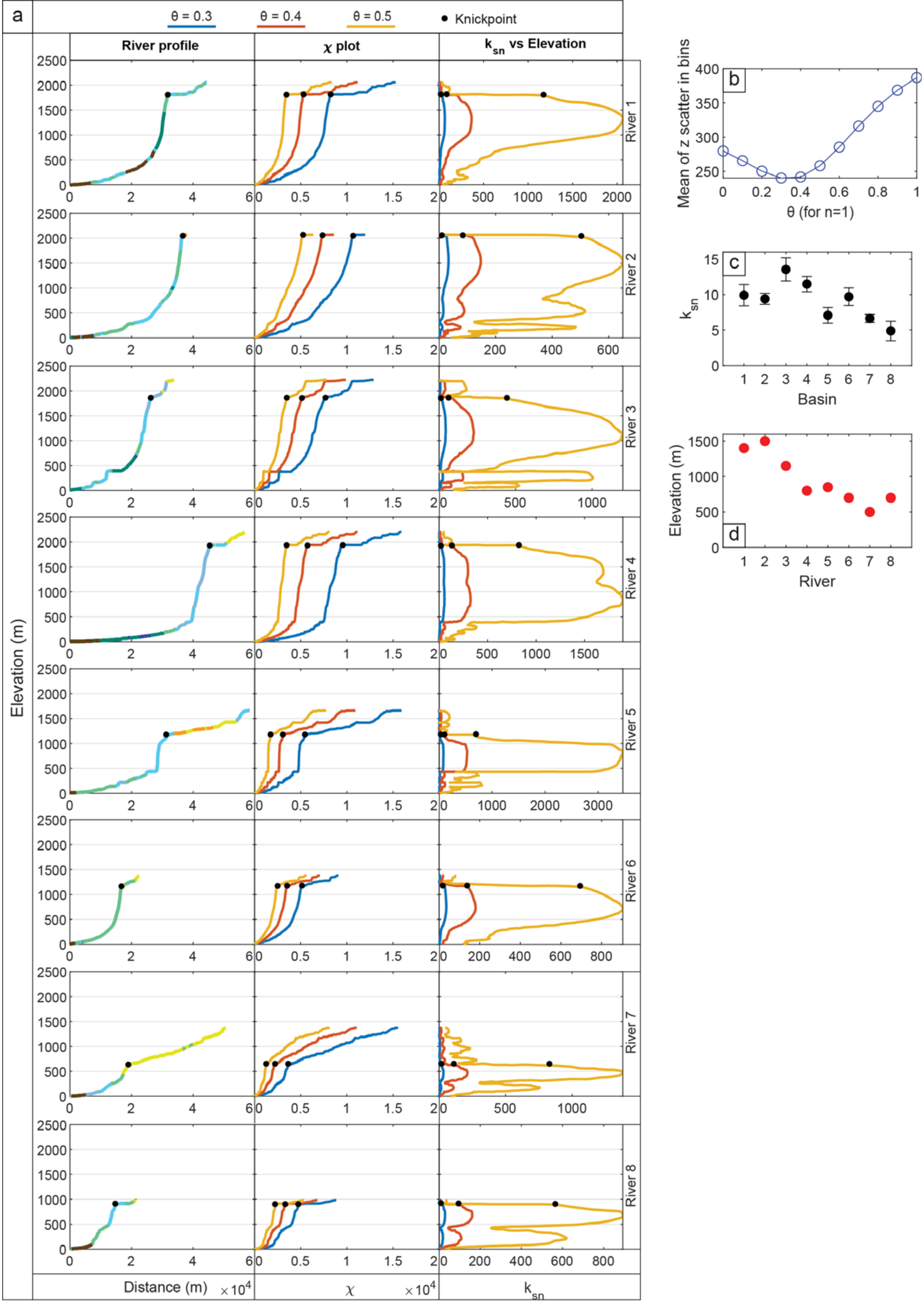

a
θ = 0.3
θ = 0.4
θ = 0.5
Knickpoint
River profile
χ plot
k_{sn} vs Elevation
Elevation (m)
River 1
River 2
River 3
River 4
River 5
River 6
River 7
River 8
Distance (m) $\times 10^4$
χ $\times 10^4$
k_{sn}
b
Mean of z scatter in bins
θ (for n=1)
c
k_{sn}
Basin
d
Elevation (m)
River

Figure 5.

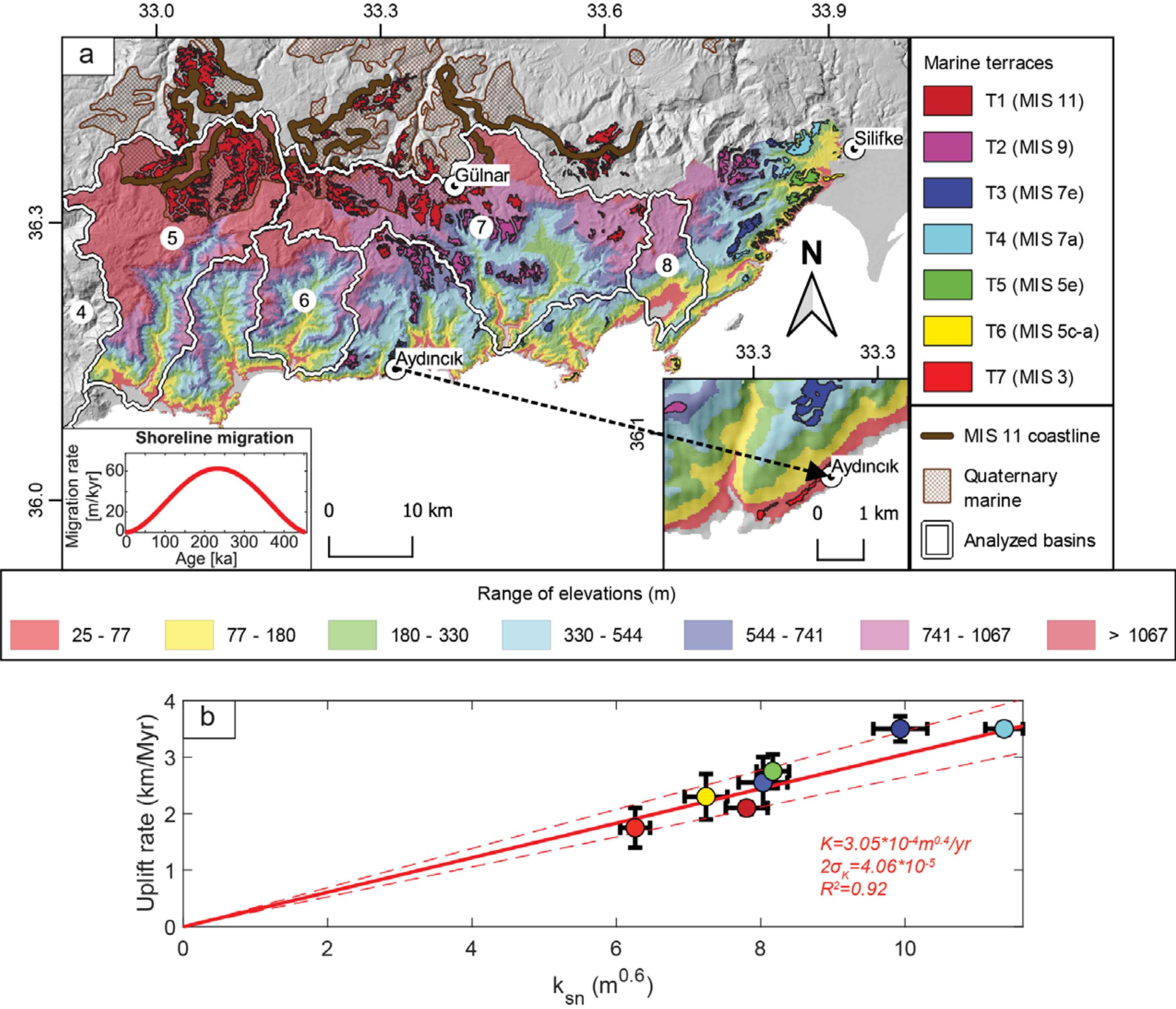

a
33.0
33.3
33.6
33.9
36.3
36.0
Silifke
Gülnar
Aydıncık
4
5
6
7
8
N
Marine terraces
T1 (MIS 11)
T2 (MIS 9)
T3 (MIS 7e)
T4 (MIS 7a)
T5 (MIS 5e)
T6 (MIS 5c-a)
T7 (MIS 3)
MIS 11 coastline
Quaternary marine
Analyzed basins
Shoreline migration
Migration rate [m/kyr]
Age [ka]
0 10 km
0 1 km
Range of elevations (m)
25 - 77
77 - 180
180 - 330
330 - 544
544 - 741
741 - 1067
> 1067
b
Uplift rate (km/Myr)
k_{sn} ($m^{0.6}$)
$K=3.05*10^{-4}m^{0.4}/yr$
$2\sigma_K=4.06*10^{-5}$
$R^2=0.92$

Figure 6.

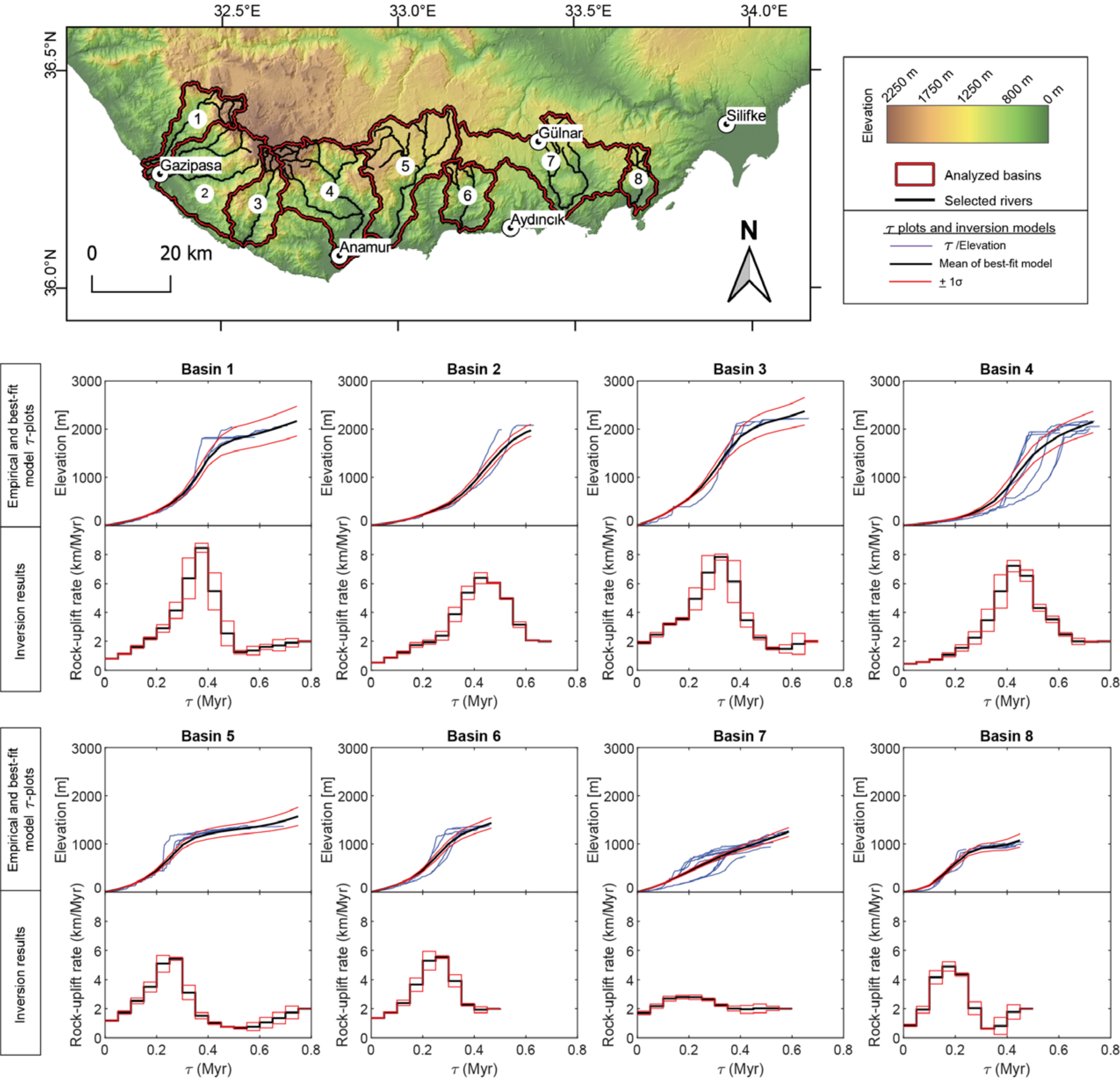

32.5°E
33.0°E
33.5°E
34.0°E
36.5°N
36.0°N
Gazipasa
Anamur
Aydıncık
Gülnar
Silifke
0
20 km
N
Elevation
2250 m
1750 m
1250 m
800 m
0 m
Analyzed basins
Selected rivers
τ plots and inversion models
τ /Elevation
Mean of best-fit model
± 1σ
Basin 1
Basin 2
Basin 3
Basin 4
Basin 5
Basin 6
Basin 7
Basin 8
Empirical and best-fit model τ-plots
Inversion results
Elevation [m]
Rock-uplift rate (km/Myr)
τ (Myr)

Figure 7.

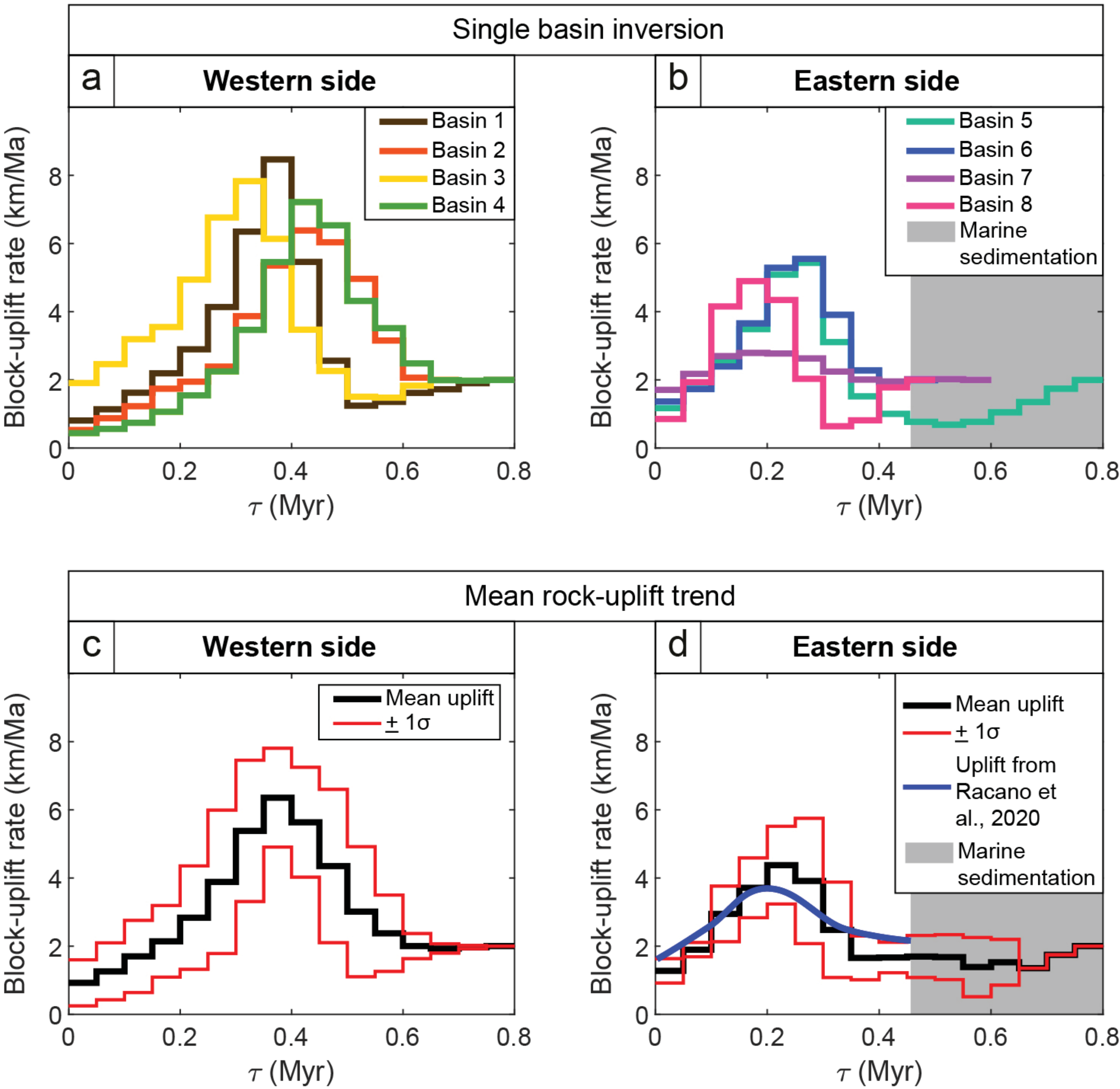
Single basin inversion
a
Western side
b
Eastern side
Basin 1
Basin 2
Basin 3
Basin 4
Basin 5
Basin 6
Basin 7
Basin 8
Marine sedimentation
Block-uplift rate (km/Ma)
τ (Myr)
Mean rock-uplift trend
c
Western side
d
Eastern side
Mean uplift
± 1σ
Uplift from Racano et al., 2020
Marine sedimentation
0
2
4
6
8
0
0.2
0.4
0.6
0.8

River Inversion setup	
K	$3.05*10^{-4}$ $m^{0.4}$/yr
2σ	$4.06*10^{-5}$
U_{pri}	0 – 4 km/Myr
n	1
θ	0.3
Reference area	$1m^2$
Drainage area of channel heads	10^6 m^2
Tsteps	50ky
MC runs	500

Figure A1.

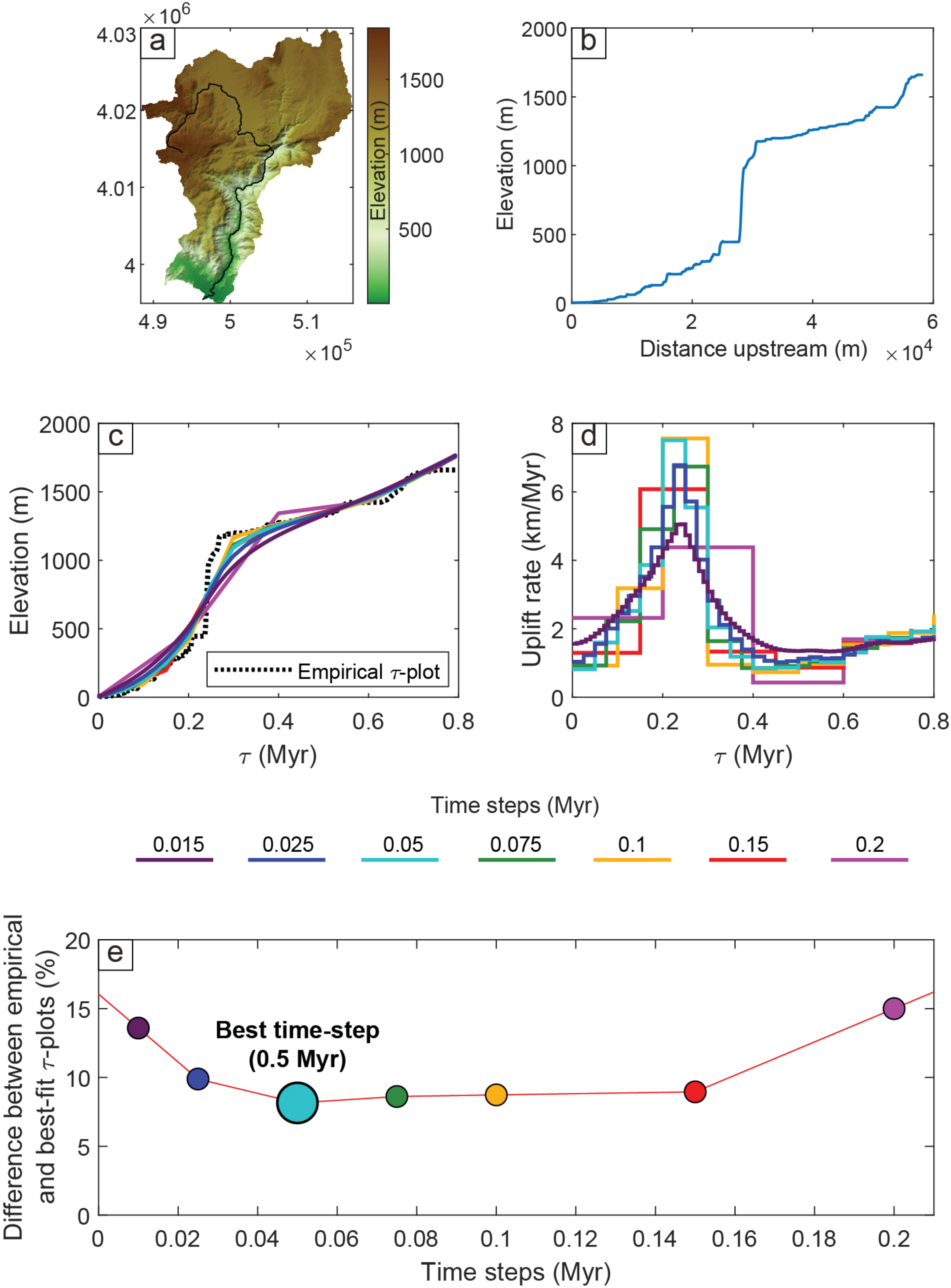

a
b
c
d
e
Elevation (m)
Distance upstream (m)
Empirical τ-plot
τ (Myr)
Uplift rate (km/Myr)
Time steps (Myr)
0.015
0.025
0.05
0.075
0.1
0.15
0.2
Difference between empirical and best-fit τ-plots (%)
Best time-step (0.5 Myr)

Figure A2.

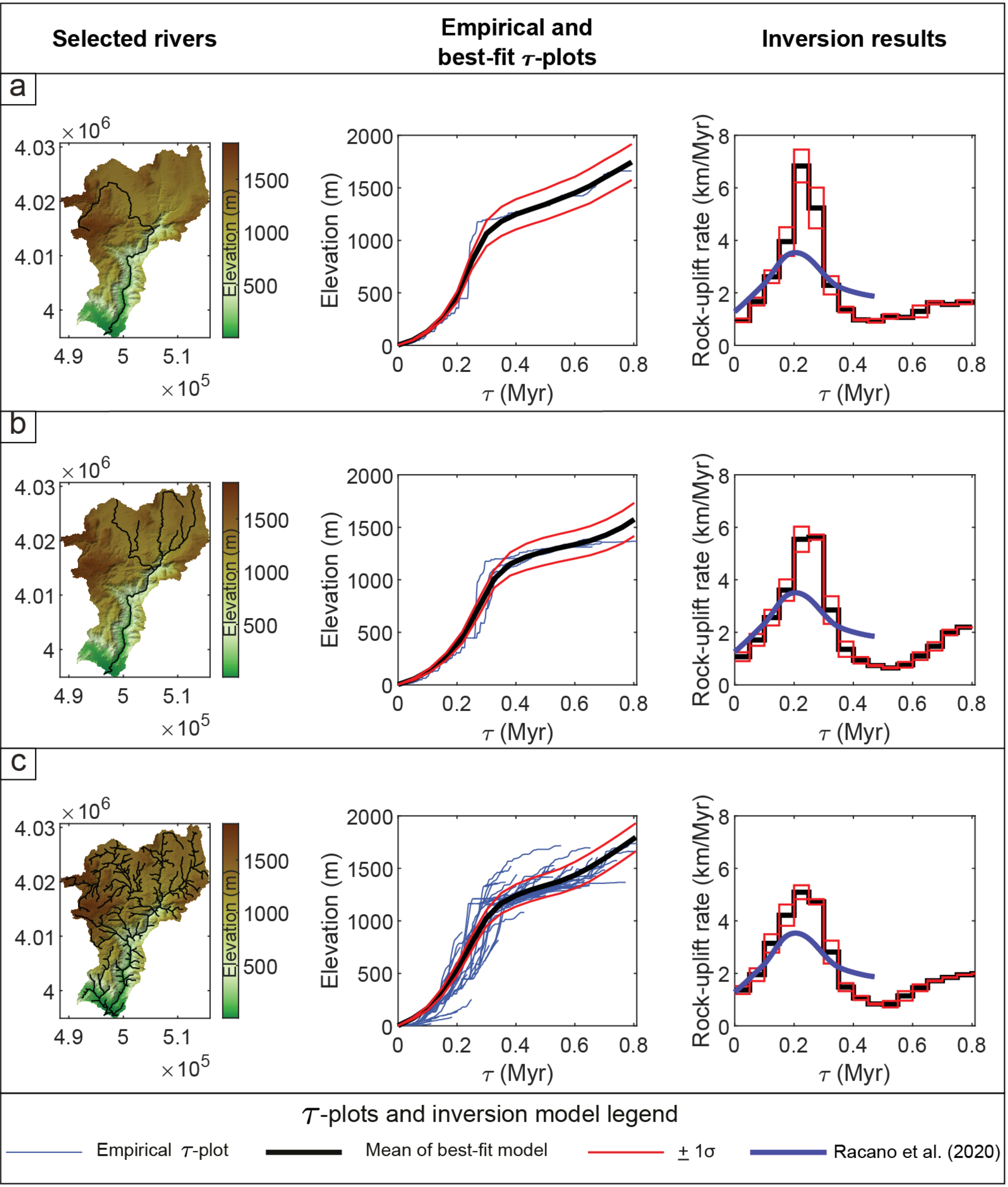

Selected rivers
Empirical and best-fit τ-plots
Inversion results
a
b
c
$\times 10^6$
4.03
4.02
4.01
4
4.9
5
5.1
$\times 10^5$
Elevation (m)
1500
1000
500
2000
0
0.2
0.4
0.6
0.8
τ (Myr)
Rock-uplift rate (km/Myr)
8
6
4
2
τ-plots and inversion model legend
Empirical τ-plot
Mean of best-fit model
± 1σ
Racano et al. (2020)

Figure A3.

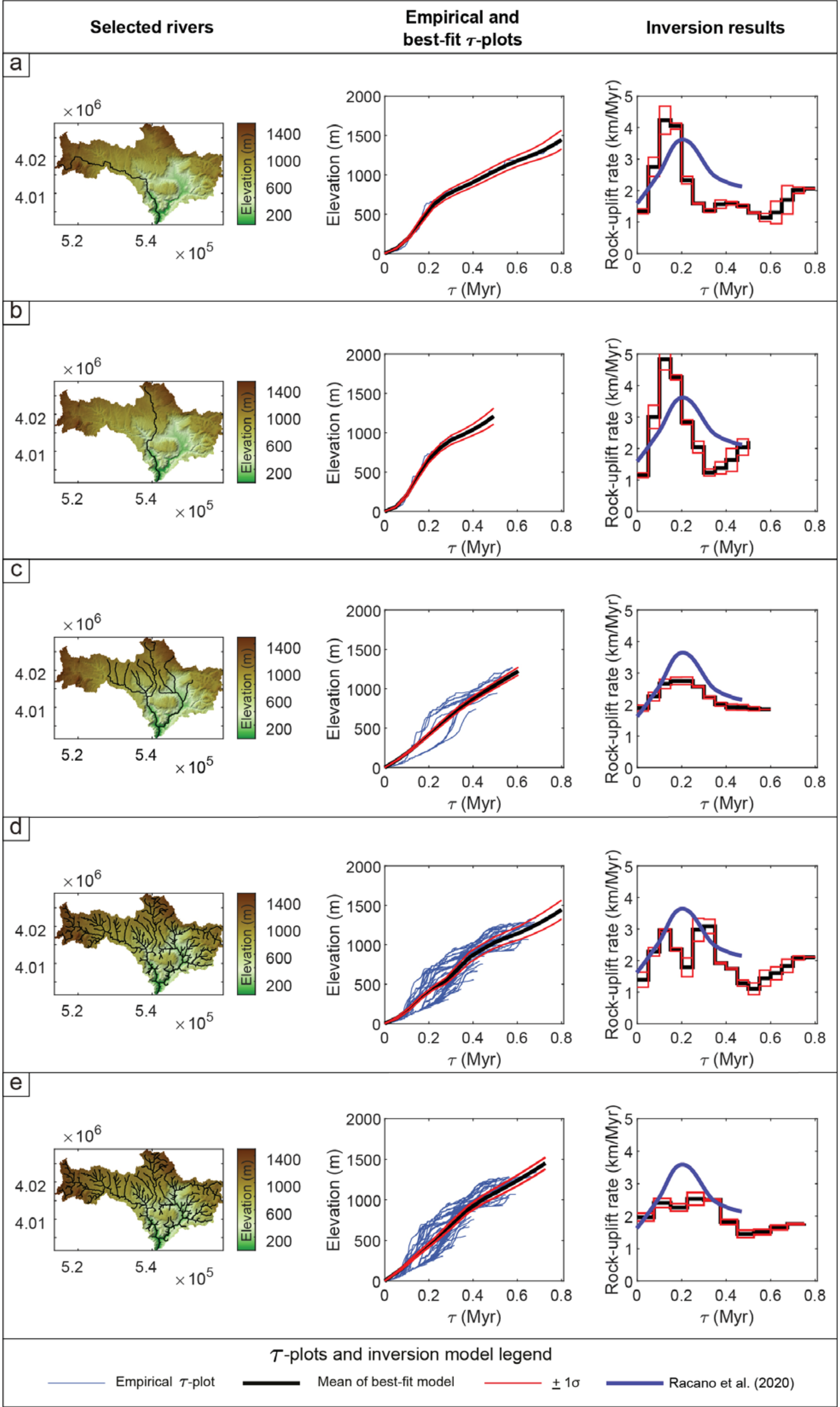
Selected rivers
Empirical and best-fit τ-plots
Inversion results
a
b
c
d
e
×10^6
4.02
4.01
5.2
5.4
×10^5
1400
1000
600
200
Elevation (m)
2000
1500
1000
500
0
0
0.2
0.4
0.6
0.8
τ (Myr)
Rock-uplift rate (km/Myr)
5
4
3
2
1
τ-plots and inversion model legend
Empirical τ-plot
Mean of best-fit model
± 1σ
Racano et al. (2020)

Figure B1.

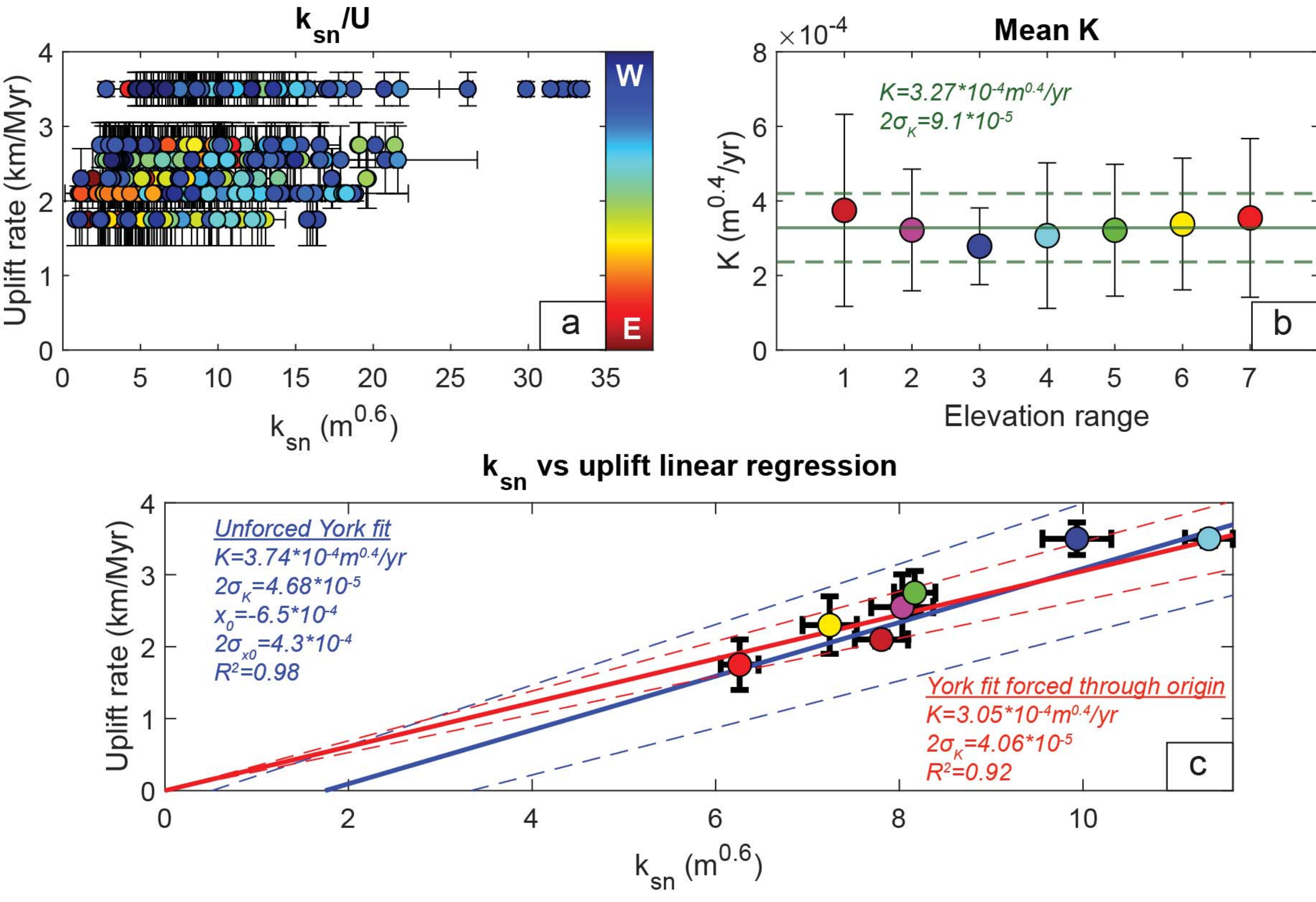

k_sn/U
Uplift rate (km/Myr)
W
E
a
k_sn (m^0.6)
Mean K
×10^-4
K=3.27*10^-4 m^0.4/yr
2σ_K=9.1*10^-5
K (m^0.4/yr)
b
Elevation range
k_sn vs uplift linear regression
Unforced York fit
K=3.74*10^-4 m^0.4/yr
2σ_K=4.68*10^-5
x_0=-6.5*10^-4
2σ_x0=4.3*10^-4
R^2=0.98
York fit forced through origin
K=3.05*10^-4 m^0.4/yr
2σ_K=4.06*10^-5
R^2=0.92
c
Uplift rate (km/Myr)
k_sn (m^0.6)

Figure B2.

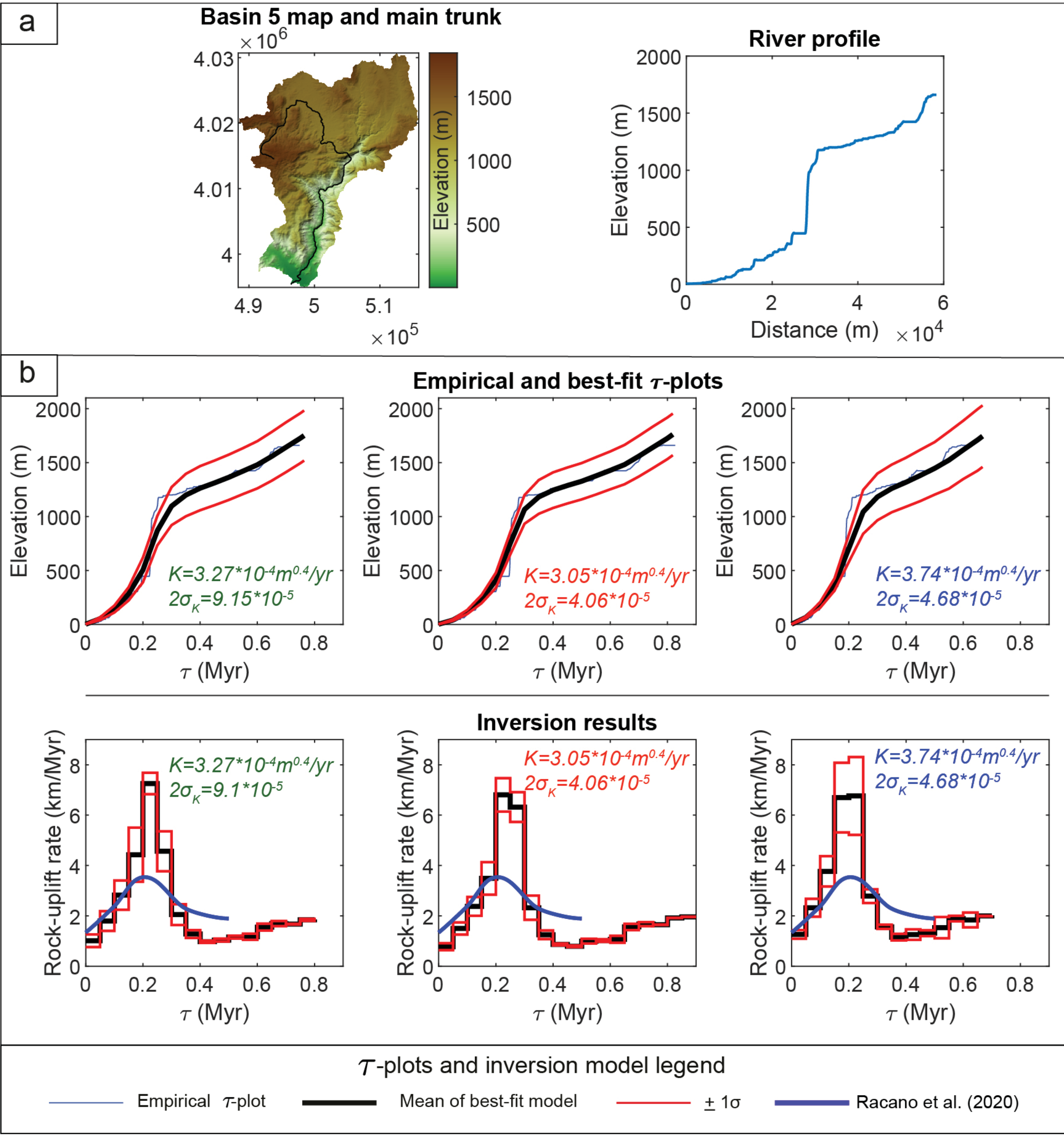

a
Basin 5 map and main trunk
Elevation (m)
River profile
Elevation (m)
Distance (m)
b
Empirical and best-fit τ-plots
Elevation (m)
τ (Myr)
K=3.27*10-4m0.4/yr
2σK=9.15*10-5
K=3.05*10-4m0.4/yr
2σK=4.06*10-5
K=3.74*10-4m0.4/yr
2σK=4.68*10-5
Inversion results
Rock-uplift rate (km/Myr)
K=3.27*10-4m0.4/yr
2σK=9.1*10-5
K=3.05*10-4m0.4/yr
2σK=4.06*10-5
K=3.74*10-4m0.4/yr
2σK=4.68*10-5
τ-plots and inversion model legend
Empirical τ-plot
Mean of best-fit model
± 1σ
Racano et al. (2020)

Figure B3.

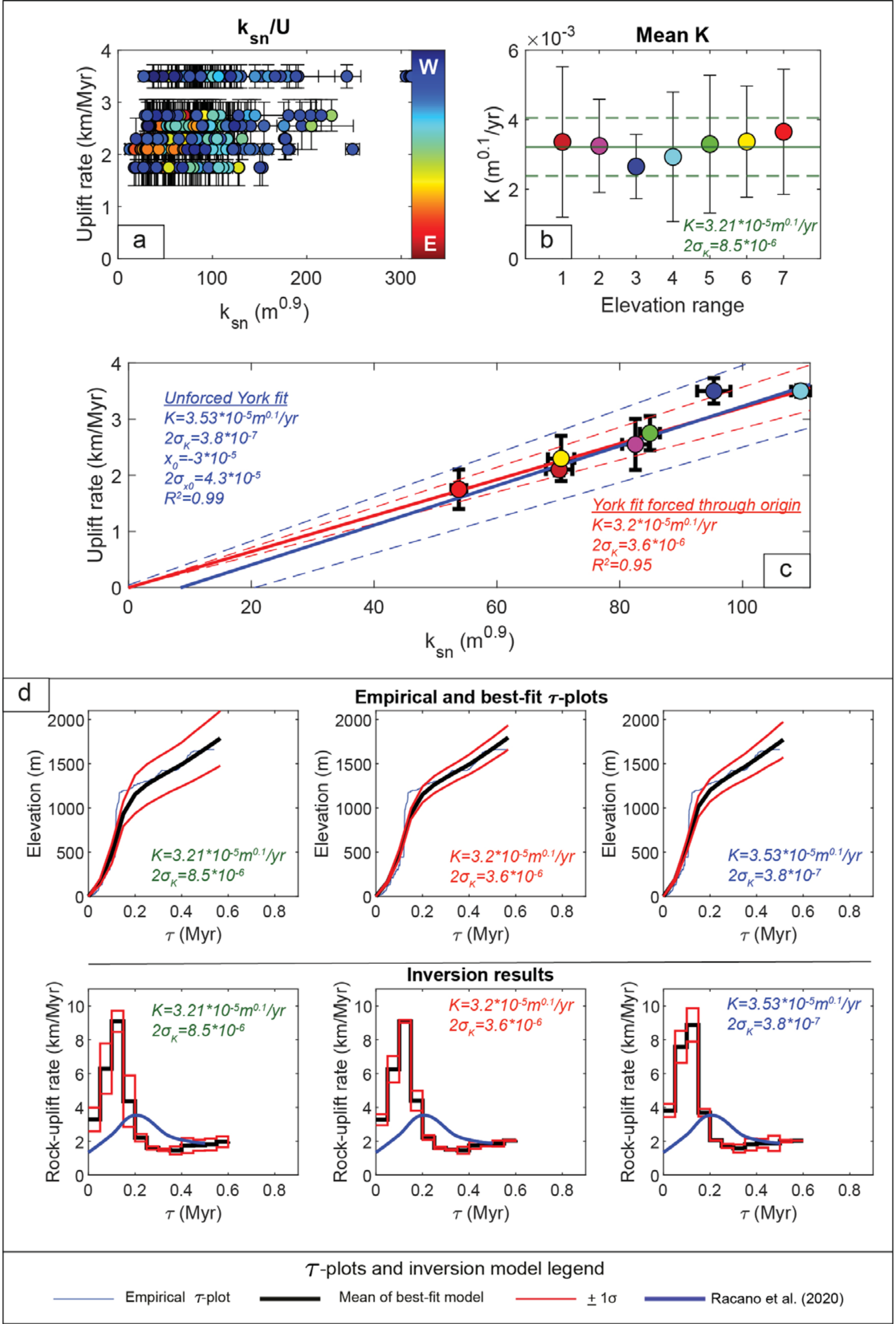

k_sn/U
Uplift rate (km/Myr)
k_sn (m^0.9)
W
E
a
Mean K
×10^-3
K (m^0.1/yr)
Elevation range
K=3.21*10^-5m^0.1/yr
2σ_K=8.5*10^-6
b
Unforced York fit
K=3.53*10^-5m^0.1/yr
2σ_K=3.8*10^-7
x_0=-3*10^-5
2σ_x0=4.3*10^-5
R²=0.99
York fit forced through origin
K=3.2*10^-5m^0.1/yr
2σ_K=3.6*10^-6
R²=0.95
c
d
Empirical and best-fit τ-plots
Elevation (m)
τ (Myr)
K=3.21*10^-5m^0.1/yr
2σ_K=8.5*10^-6
K=3.2*10^-5m^0.1/yr
2σ_K=3.6*10^-6
K=3.53*10^-5m^0.1/yr
2σ_K=3.8*10^-7
Inversion results
Rock-uplift rate (km/Myr)
τ-plots and inversion model legend
Empirical τ-plot
Mean of best-fit model
± 1σ
Racano et al. (2020)

Figure B4.

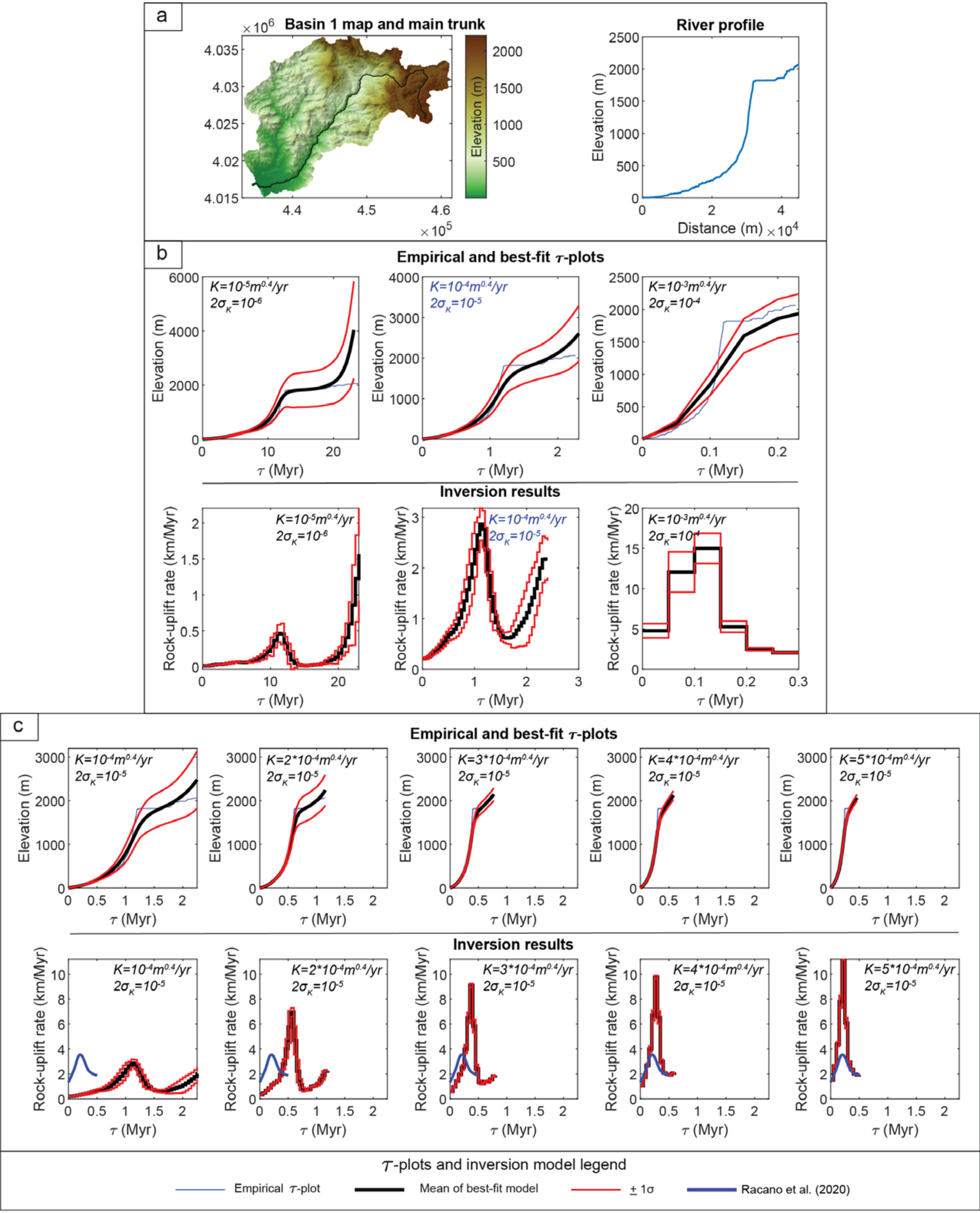
a
Basin 1 map and main trunk
River profile
Elevation (m)
Distance (m)
b
Empirical and best-fit τ-plots
$K=10^{-5}m^{0.4}/yr$ $2\sigma_K=10^{-6}$
$K=10^{-4}m^{0.4}/yr$ $2\sigma_K=10^{-5}$
$K=10^{-3}m^{0.4}/yr$ $2\sigma_K=10^{-4}$
τ (Myr)
Inversion results
Rock-uplift rate (km/Myr)
c
Empirical and best-fit τ-plots
$K=2*10^{-4}m^{0.4}/yr$ $2\sigma_K=10^{-5}$
$K=3*10^{-4}m^{0.4}/yr$ $2\sigma_K=10^{-5}$
$K=4*10^{-4}m^{0.4}/yr$ $2\sigma_K=10^{-5}$
$K=5*10^{-4}m^{0.4}/yr$ $2\sigma_K=10^{-5}$
Inversion results
τ-plots and inversion model legend
Empirical τ-plot
Mean of best-fit model
± 1σ
Racano et al. (2020)